NUREG/CR-6380
ORNL/TM-13091

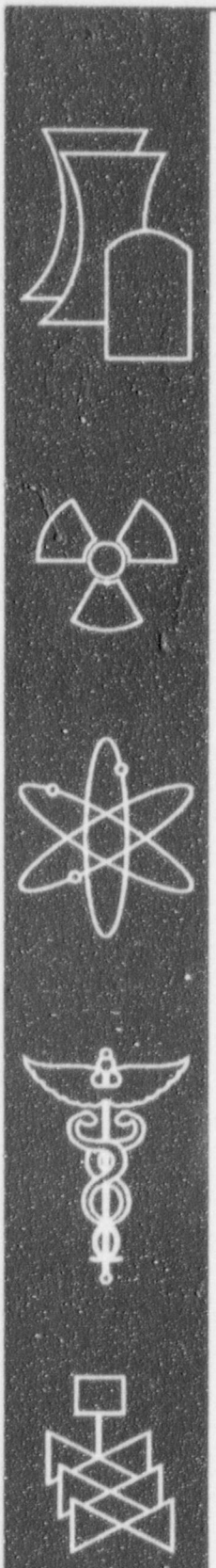

Assessment of the Fracture Behavior of Weld Material in Full-Thickness Clad Beams

Oak Ridge National Laboratory

U.S. Nuclear Regulatory Commission
Office of Nuclear Regulatory Research
Washington, DC 20555-0001

NUREG/CR-6380
ORNL/TM-13091

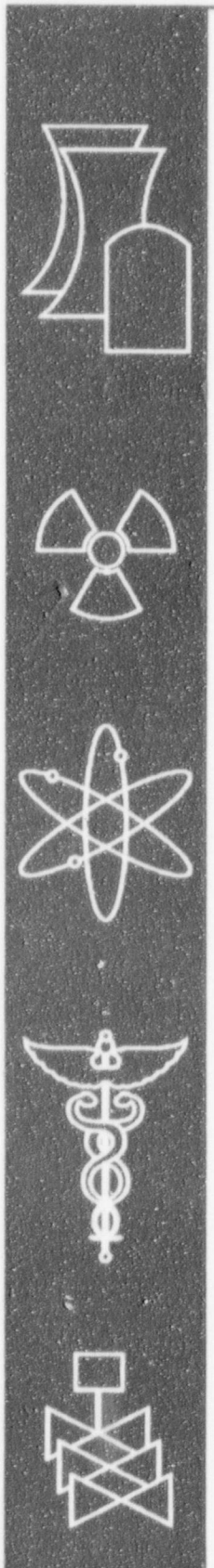

Assessment of the Fracture Behavior of Weld Material in Full-Thickness Clad Beams

Oak Ridge National Laboratory

U.S. Nuclear Regulatory Commission
Office of Nuclear Regulatory Research
Washington, DC 20555-0001

NUREG/CR-6380
ORNL/TM-13091

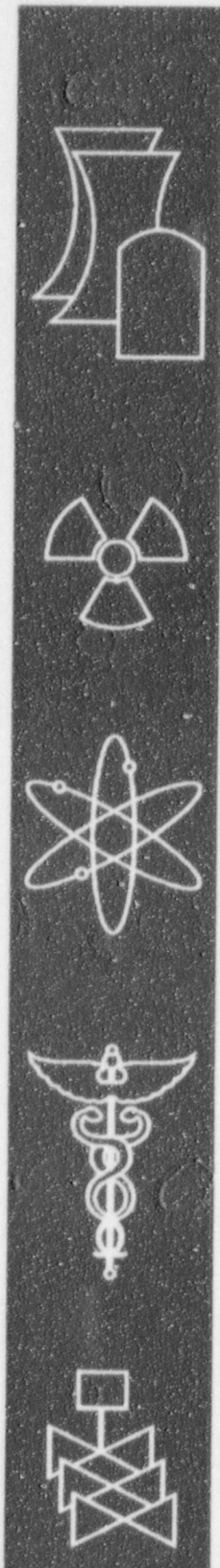

Assessment of the Fracture Behavior of Weld Material in Full-Thickness Clad Beams

Oak Ridge National Laboratory

U.S. Nuclear Regulatory Commission
Office of Nuclear Regulatory Research
Washington, DC 20555-0001

AVAILABILITY NOTICE

Availability of Reference Materials Cited in NRC Publications

NRC publications in the NUREG series, NRC regulations, and *Title 10, Energy,* of the *Code of Federal Regulations,* may be purchased from one of the following sources:

1. The Superintendent of Documents
   U.S. Government Printing Office
   P.O. Box 37082
   Washington, DC 20402–9328
   <http://www.access.gpo.gov/su_docs>
   202–512–1800

2. The National Technical Information Service
   Springfield, VA 22161–0002
   <http://www.ntis.gov/ordernow>
   703–487–4650

The NUREG series comprises (1) brochures (NUREG/BR-XXXX), (2) proceedings of conferences (NUREG/CP-XXXX), (3) reports resulting from international agreements (NUREG/IA-XXXX), (4) technical and administrative reports and books [(NUREG-XXXX) or (NUREG/CR-XXXX)], and (5) compilations of legal decisions and orders of the Commission and Atomic and Safety Licensing Boards and of Office Directors' decisions under Section 2.206 of NRC's regulations (NUREG-XXXX).

A single copy of each NRC draft report is available free, to the extent of supply, upon written request as follows:

Address: Office of the Chief Information Officer
Reproduction and Distribution
Services Section
U.S. Nuclear Regulatory Commission
Washington, DC 20555–0001
E–mail: <DISTRIBUTION@nrc.gov>
Facsimile: 301–415–2289

A portion of NRC regulatory and technical information is available at NRC's World Wide Web site:

<http://www.nrc.gov>

All NRC documents released to the public are available for inspection or copying for a fee, in paper, microfiche, or, in some cases, diskette, from the Public Document Room (PDR):

NRC Public Document Room
2120 L Street, N.W., Lower Level
Washington, DC 20555–0001
<http://www.nrc.gov/NRC/PDR/pdr1.htm>
1–800–397–4209 or locally 202–634–3273

Microfiche of most NRC documents made publicly available since January 1981 may be found in the Local Public Document Rooms (LPDRs) located in the vicinity of nuclear power plants. The locations of the LPDRs may be obtained from the PDR (see previous paragraph) or through:

<http://www.nrc.gov/NRC/NUREGS/SR1350/V9/lpdr/html>

Publicly released documents include, to name a few, NUREG-series reports; *Federal Register* notices; applicant, licensee, and vendor documents and correspondence; NRC correspondence and internal memoranda; bulletins and information notices; inspection and investigation reports; licensee event reports; and Commission papers and their attachments.

Documents available from public and special technical libraries include all open literature items, such as books, journal articles, and transactions, *Federal Register* notices, Federal and State legislation, and congressional reports. Such documents as theses, dissertations, foreign reports and translations, and non-NRC conference proceedings may be purchased from their sponsoring organization.

Copies of industry codes and standards used in a substantive manner in the NRC regulatory process are maintained at the NRC Library, Two White Flint North, 11545 Rockville Pike, Rockville, MD 20852–2738. These standards are available in the library for reference use by the public. Codes and standards are usually copyrighted and may be purchased from the originating organization or, if they are American National Standards, from—

American National Standards Institute
11 West 42nd Street
New York, NY 10036–8002
<http://www.ansi.org>
212–642–4900

NUREG/CR-6380
ORNL/TM-13091

Assessment of the Fracture Behavior of Weld Material in Full-Thickness Clad Beams

Manuscript Completed: February 1999
Date Published: July 1999

Prepared by
J. A. Keeney, B. R. Bass, W. J. McAfee,
P. T. Williams

Oak Ridge National Laboratory
Managed by Lockheed Martin Energy Research Corp.

Oak Ridge National Laboratory
Oak Ridge, TN 37831-6285

S. N. Malik, NRC Project Manager

Prepared for
Division of Engineering Technology
Office of Nuclear Regulatory Research
U.S. Nuclear Regulatory Commission
Washington, DC 20555-0001
NRC Job Code B0119

Abstract

A Heavy-Section Steel Technology testing program was conducted on full-thickness clad beam specimens fabricated using material from the reactor pressure vessel (RPV) of a canceled nuclear power plant to generate fracture toughness data for both deep and shallow cracks in prototypic RPV material. The beam specimens incorporated weld, base, and overlay cladding materials. Factors influencing the fracture toughness of RPV material containing shallow cracks include crack-tip constraint, material property gradients, weld inhomogeneities, the cladding process, and residual stresses.

In the first testing phase, five full-thickness clad beam specimens were fabricated with through-thickness cracks that ranged in depth from 10 to 114 mm ($0.05 \leq a/W \leq 0.5$) in the weld material. These specimens were tested in three-point bending at temperatures in the transition region of the weld metal fracture toughness curve ($T - NDT$ about 25°C). Fracture toughness estimates were obtained from load versus load-line displacement and crack-mouth opening displacement data using finite-element techniques and estimation schemes based on the η-factor method.

One of the beams experienced a significant amount of precleavage stable ductile tearing. Effects of precleavage ductile tearing on fracture toughness were investigated using a continuum damage model based on the Gurson-Tvergaard formulation. The inclusion of residual stress estimates had a measurable effect on the shallow-crack toughness data. The cleavage toughness data were compared with other shallow- and deep-crack uniaxial beam data generated previously from plate material that conformed to SA533, Grade B material specification requirements. The range in scatter for data obtained from the clad beam specimens is consistent with that from the laboratory-scale single-edge-notched-bend (SENB) specimens tested at the same temperature. The minimum toughness value from the clad beam specimens was provided by a shallow-crack beam, not by the single deep-cracked beam tested in this series. However, the machined flaw, and thus the sharpened crack tip, for this specimen was near the weld/base heat-affected-zone (HAZ). Even though no metallurgical investigation of the exact crack tip location has been performed, it is possible that the toughness value obtained is not representative of the bulk weld metal. At this time, however, this toughness result is being treated as valid. Additional full-thickness clad beam specimens that were tested with shallow cracks located in prototypical full-thickness RPV plate material are being evaluated to complete the investigation.

Contents

List of Figures

List of Tables

Acronyms

ABI	Automated Ball Indentation
ANSI	American National Standards Institute
ASME	American Society of Mechanical Engineers
ASTM	American Society of Testing and Materials
CVN	Charpy V-notch
CMOD	crack-mouth-opening displacement
CT	compact tension
DOE	Department of Energy
EDM	electro-discharge machining
G-T	Gurson-Tvergaard
HAZ	heat-affected zone
HSST	Heavy Section Steel Technology
LLD	load-line displacement
LN_2	liquid nitrogen
NDE	nondestructive examination
NIST	National Institute for Standards and Technology
NRC	Nuclear Regulatory Commission
ORNL	Oak Ridge National Laboratory
PFM	probabilistic fracture-mechanics
PTS	pressurized-thermal shock
RPV	reactor pressure vessel
RT_{NDT}	reference nil-ductility temperature
SENB	single-edge-notched bend
SSY	small-scale yielding
SGMM	simplified Gurson material model
TGM	thermal gradient method

1 Introduction

1.1 Background

Evaluations of reactor pressure vessel (RPV) integrity under pressurized-thermal shock (PTS) loading are based on the following:

- the Marshall flaw distribution,[1]
- U.S. Nuclear Regulatory Commission (NRC) Guide 1.154,[2] and
- data from deep-crack fracture toughness specimens.

The Marshall flaw distribution predicts more small flaws than large flaws; NRC Regulatory Guide 1.154 requires that all flaws be considered surface flaws. Probabilistic fracture-mechanics (PFM) analyses of RPVs indicate that a high percentage of the cracks that are predicted to fracture by cleavage initiate from shallow flaws.[3] Because the postulated existence of shallow flaws has a dominant influence on the results of PFM analyses and ultimately on the conditional probability of vessel failure in a PTS evaluation, the shallow surface crack is very important in RPV structural integrity assessments.

1.2 Purpose

This report describes preliminary results from a Heavy Section Steel Technology (HSST) testing program designed to investigate some of the effects on fracture toughness of the conditions outlined above. In the initial phase of the investigation, five full-thickness clad beam specimens were fabricated at Oak Ridge National Laboratory (ORNL) and tested at the National Institute for Standards and Technology (NIST), Gaithersburg, Maryland.* Material used to fabricate the test specimens was obtained from a RPV of a canceled nuclear power plant.

These tests were performed to investigate the influence of metallurgical gradients, weld inhomogeneities, and the cladding process on the fracture toughness of material containing shallow cracks. Specifically, fracture toughness data were generated from three-point arc-bend test specimens (229- by 226-mm cross section and ~1300-mm chord length) fabricated from full-thickness RPV clad, weld, and base material shell segments. Shallow cracks in these beams were located in the weld material.

Comparison of results from these tests with those from homogeneous shallow-crack test specimens[4] provides an opportunity to quantify the effects of certain near-surface conditions on fracture toughness. In addition, the effective fracture toughness from these large beams can be compared with the toughness as defined by current rules[5] provided in Section XI of the American Society of Mechanical Engineers (ASME) Boiler and Pressure Vessel Code.

1.3 Scope

Chapter 2 provides a summary of the HSST full-thickness clad beam testing program, including a description of specimen geometry, material characterization studies, testing procedures, experimental results, and comparisons with other shallow-crack fracture toughness data.

Analyses of the test data, including comparisons of test data with finite-element analysis results and applications of toughness estimation techniques, are described in Chap. 3. Applications of stress-based constraint characterizations developed by O'Dowd and Shih[6-8] to the clad beam data are also included in Chap. 3.

A summary and preliminary conclusions, together with a review of future plans for the clad beam testing program, are given in Chap. 4.

*NIST Test Report for Full-Thickness Clad Beam Fracture-Toughness Test
Bendbar #1 tested April 6, 1993 (report dated March 10 1994);
Bendbar #2 tested January 13, 1994 (report dated March 10, 1994);
Bendbar #3 tested February 24,1994 (report dated March 21, 1994);
Bendbar #4 tested August 24,1994 (report dated December 23, 1994);
Bendbar #5 tested September 1,1994 (report dated December 23, 1994).

2 Full-Thickness Clad Beam Testing Program

2.1 Test Specimen

The full-thickness clad beam specimens were fabricated from an RPV shell segment that was available from a canceled pressurized-water nuclear power reactor. The plant was canceled during construction, so the vessel was never placed into service. A sketch of the vessel shell segment is shown in Fig. 2.1.

The shell segment includes two circumferential welds and one longitudinal weld. The "lower" circumferential weld connects two shell courses, and the "upper" circumferential weld connects a shell course with the nozzle ring. The longitudinal weld is located near the mid-width of the shell segment and runs from the "upper" circumferential weld through the lower end of the shell segment.

The RPV base material conformed to SA 533, Grade B material specification requirements. The welds were submerged-arc welds (SAW) utilizing the same weld procedure and the same heat of A 533 B class 1 filler metal.* For the circumferential welds, the root pass at the inside surface of the vessel wall was removed by grinding to sound material and back-welded by hand. The back-fill welds were thus performed using a different process† and heat of weld wire. To check this information, chemistry determinations were performed on the longitudinal weld, the circumferential weld, and the circumferential back-fill welds. It was found that the longitudinal and circumferential weld had the same chemistry whereas the circumferential back-fill weld exhibited significant variation in several elements. After assembly, the inner surface of the RPV was clad with a stainless steel weld overlay. The base, clad overlay, and weld materials are prototypic of a production-quality RPV. The shell has a nominal inner radius of 2210 mm (87 in.) and a thickness of 232 mm (9.125 in.) that includes ~5 mm (~0.2 in.) of clad overlay.

Because the first five-specimen series was intended to investigate the fracture behavior of the longitudinal weld material, the test beams were cut in the circumferential direction of the shell. A longitudinal master blank with a length sufficient to fabricate five test beams was first flame-cut from the shell using the cut-up plans shown in Fig. 2.2. Five blanks were then abrasive-cut from the master blank. Abrasive-cutting was used at this stage to ensure that any material affected by the flame-cutting would not be contained in the test beams. Figure 2.3 shows one of the beam blanks before final machining. The weld location was polished and etched to accurately locate the centerline of the weld joining the two beam halves. This centerline was then marked for machining reference.

A circumferential coupon containing the test material was removed from the master blank during the process of cutting the test beam blanks. Metallurgical details of the coupon can be seen in Fig. 2.4. The base material, the weld material with its multiple layers, the heat-affected zone (HAZ) between the weld and base materials, and the clad layer with its HAZ are clearly visible.

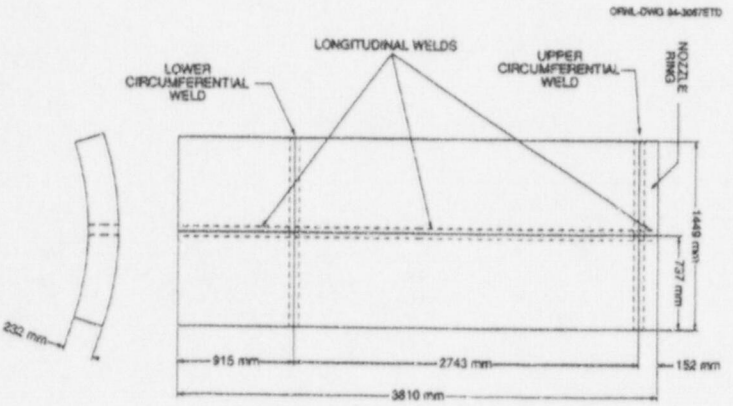

Figure 2.1 Sketch of RPV shell segment used as source material for full-thickness clad beam specimens

* Letter from Stephen T. Byrne, ABB Combustion Engineering, to W. E. Pennell, Oak Ridge National Laboratory, April 1, 1998.

† Personal communication from Stephen T. Byrne, ABB Combustion Engineering, to W. J. McAfee, Oak Ridge National Laboratory, December 1, 1998.

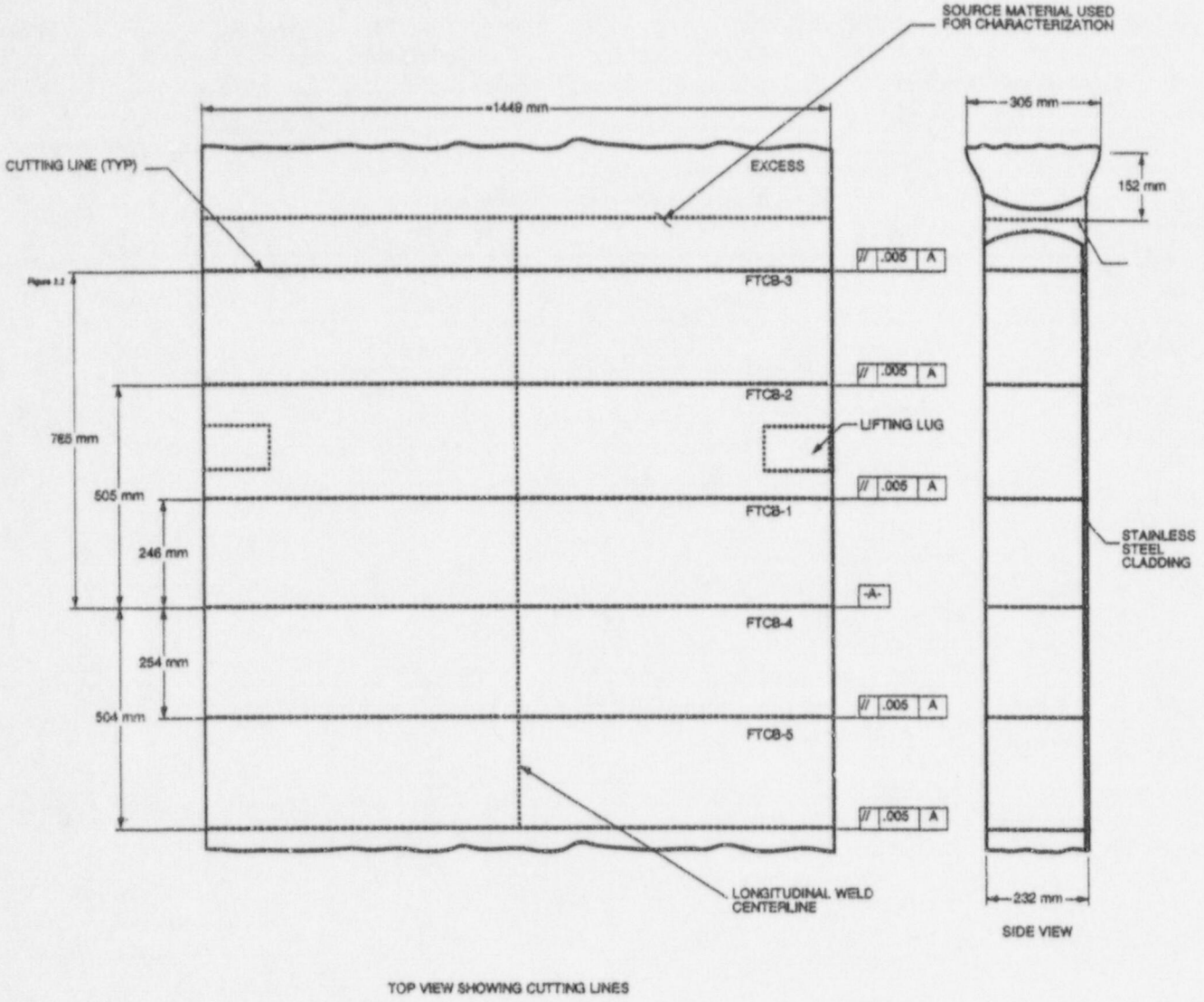

Figure 2.2 Cut-up plan for full-thickness clad beam blanks.

ORNL-PHOTO 8317-92

Figure 2.3 Full-thickness clad beam blank before final machining

ORNL-PHOTO 8083-94

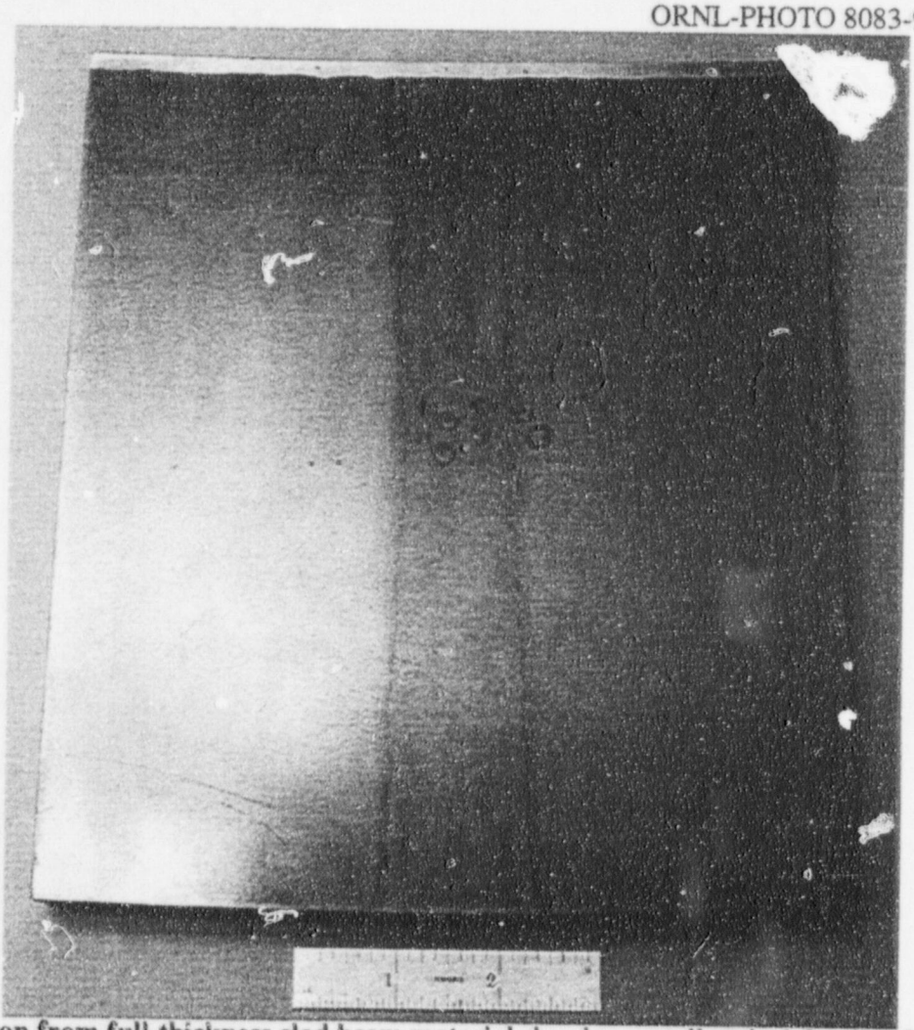

Figure 2.4 Coupon from full-thickness clad beam material showing metallurgical details of test weld

Full-Thickness

After abrasive-cutting, the specimens were machined to final dimensions, incorporating handling, load-contact, and flaw details. A sketch of the specimen geometry is shown in Fig. 2.5. The specimen was designed to be tested in three-point bending with a load span (S) of 1219.2 mm (48 in.). Flat parallel-load contact points were machined on the top and bottom surfaces of the beam to remove surface irregularities and to ensure uniform load application across the width of the beam. The centerline of the weld was located and used as a reference in machining the specimen details such that a radial plane, nominally passing through the center of the weld, would be a plane of symmetry for the specimen.

The flaw was machined to lie in this plane using the wire electro-discharge machining (EDM) process and extended from the shell inner surface, i.e., the clad surface, to a predetermined depth into the beam. The EDM process allows flaws with a very narrow width (0.5 mm) and uniform depth to be machined into thick sections with minimum impact on the surrounding material. Heating and the associated potential for introduction of surface residual stresses is minimized using this method, and only small amounts of material are removed.

Final dimensions for each clad beam specimen are shown in Table 2.1. Note that the flaw in each beam was machined to a different depth. One deep-flaw specimen (CB-1.1) and four shallow-flaw specimens (CB-1.2 through CB-1.5) were produced. The crack depth , a, listed for each beam is the final depth after fatigue precracking. Fatigue precracking details are provided in Sect. 2.2.

The shell contained both axial (longitudinal) and circumferential welds. In the course of cutting the beam blanks, the upper circumferential weld was made available for material characterization. Tests, using the Automated Ball Indentation (ABI) technique,[9] indicated that the tensile properties of the axial and circumferential weld are similar. The characterization of the circumferential weld included Charpy V–notch (CVN) tests, reference nil-ductility temperature (RT_{NDT}) determinations[10], and tensile tests (at temperatures ranging from -80 °C to 23 °C). A complete description of the circumferential weld characteristics has been previously reported.[11]

The impact and tensile material characterization data were used to develop a consistent set of material properties needed for test data evaluation and finite-element analyses of the clad beams. These properties are shown in Table 2.2. The ABI technique was used to determine the yield stress for the weld material, as plotted in Fig. 2.6. The tabulated yield stress for the weld material is 36 % higher than the yield stress for the base material.

2.2 Test Equipment and Procedures

The full-thickness clad beam tests were performed at NIST using the 53.4 MN (12000 kips) servo-hydraulic test machine. A three-point bend fixture with span and load capacity sufficient to perform these tests was designed and fabricated. This fixture was designed for a load capacity of at least 15 MN (3370 kips), which was calculated to be in excess of that required for these tests. Because the tests were performed at a low temperature, an environmental chamber was fabricated to completely enclose the test specimen and load-contact points to facilitate control of both time- and spatially-dependent temperature variations in the specimen.

The total test sequence for the set of five beams involved the following three phases:

- shakedown and demonstration,
- fatigue precracking, and
- failure test.

As indicated by the footnote in Table 2.1, the deep-flaw specimen was designated as a development beam for this series. The primary purpose of the development beam test was to verify and validate the testing procedures for the remaining tests. This beam was sent to NIST in blank form, i.e., before final machining and without a notch or crack. It was instrumented with 16 thermocouples, shown schematically in Fig. 2.7, and mounted in the test facility with the environmental enclosure in place. The beam was then cooled as it would be for an actual fracture test, and measurements of cooling rate and temperature distribution were made. Cooling was achieved by a spray of liquid nitrogen (LN_2) onto the beam surface. A procedure was developed whereby the beam would be cooled to about 5 °C below the target test temperature, the LN_2 spray would be stopped, and the beam would then be allowed to thermally equilibrate and warm to the test temperature. This procedure was selected because the change in temperature during the fracture test was considered acceptable. After these demonstration tests were completed, this beam was sent to the machine shop for final machining into the fracture test specimen CB-1.1.

When CB-1.1 was returned as a test specimen, it was fully instrumented with crack-mouth-opening-displacement (CMOD) gages, as shown in Fig. 2.8, and surface strain

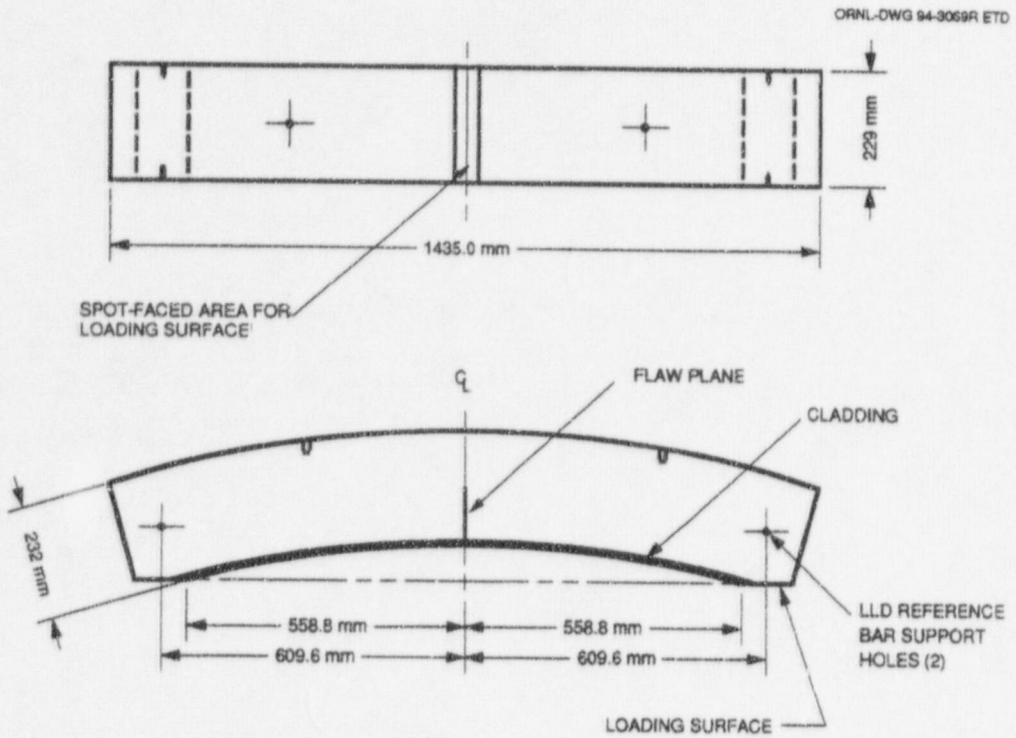

Figure 2.5 Sketch of full-thickness clad beam specimen

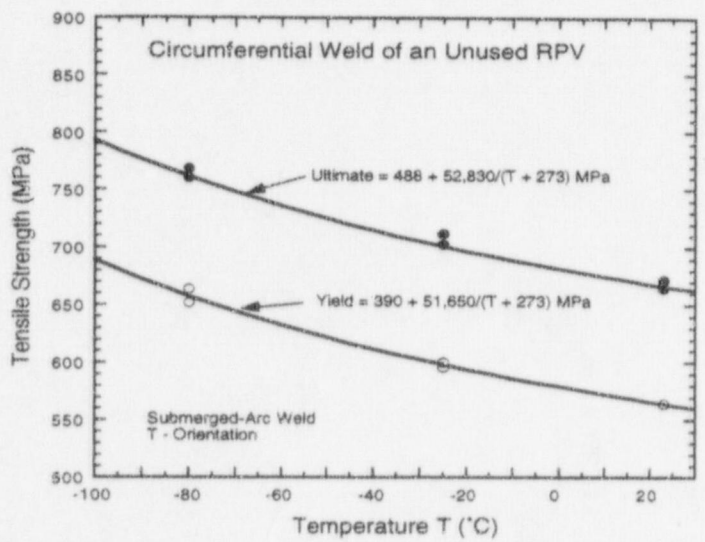

Figure 2.6 Yield and ultimate tensile strength of circumferential weld material.

Table 2.1 Specimen geometry of full-thickness clad beam specimens

Parameter	CB-1.1[a]	CB-1.2	CB-1.3	CB-1.4	CB-1.5
Load span, S (mm)	1219.2	1219.2	1219.2	1219.2	1219.2
Thickness[b], B (mm)	230.2	230.2	229.6	229.1	231.6
Width, W (mm)	225.7	224.3	224.3	228.9	225.0
Crack depth, a (mm)	117.5	10.8	23.7	22.6	12.1
Ratio, a/W	0.50	0.05	0.10	0.10	0.05

[a]Used as development beam.
[b]Thickness includes ~5 mm of clad overlay.

Table 2.2 Material properties at test temperature of -25 °C

Property	Base Material	Weld Material	Cladding Overlay
Modulus of elasticity (E), MPa	200,000	200,000	152,000[a]
Poisson's ration (v)	0.3	0.3	0.3
Yield Strength (σ_0), MPa	440[b]	599[c]	367[b]
Ultimate strength (σ_u), MPa	660[d]	704[e]	659
RT_{NDT}, °C		-23	
NDT, °C		-50	

[a]Measured E value from S. K. Iskander et al., Martin Marietta Energy Systems, Inc., Oak Ridge National Laboratory, "Experimental Results of Tests to Investigate Flaw Behavior of Mechanically Loaded Stainless Steel Clad Plates," NUREG/CR-5785 (ORNL/TM-11950) April 1992.
[b]σ_0 measured by ABI technique.
[c]Evaluated from $\sigma_0 = 390 + 51650 / (T + 273)$ where T is the material temperature in °C.
[d]σ_u measured by Rockwell B indentation technique.
[e]Evaluated from $\sigma_u = 488 + 52830 / (T + 273)$.

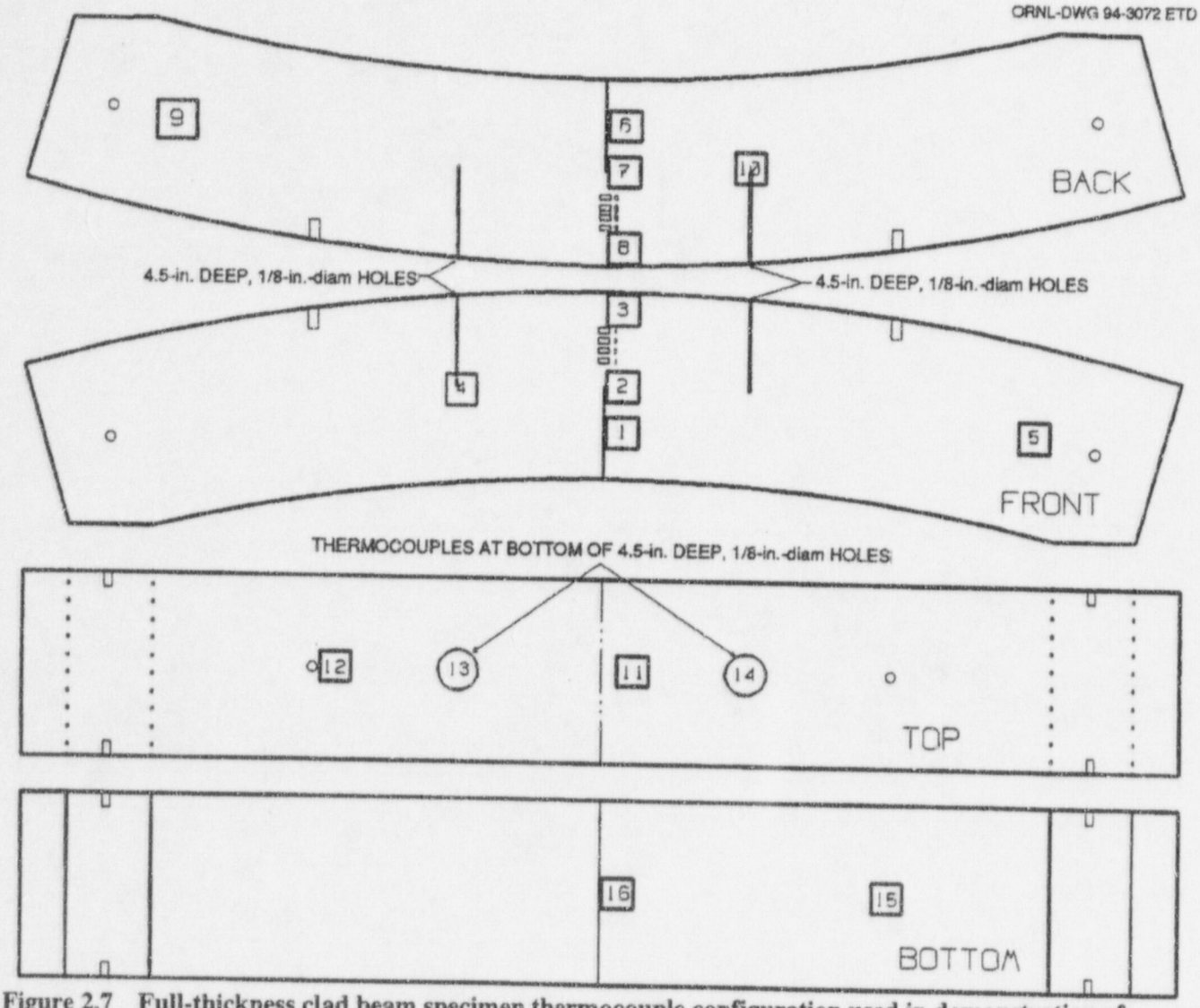

Figure 2.7 Full-thickness clad beam specimen thermocouple configuration used in demonstration of temperature control.

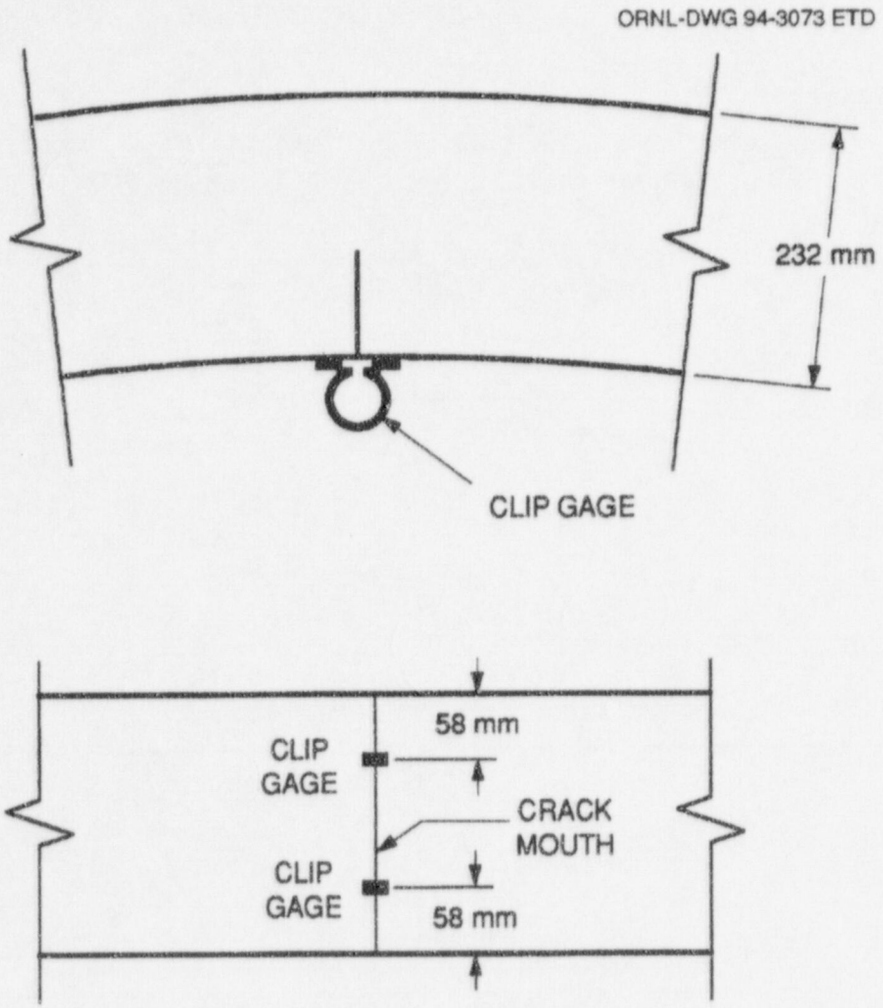

Figure 2.8 Location of crack-mouth-opening clip gages used on clad beam.

gages and thermocouples, as shown in Fig. 2.9. In addition, a specially designed fixture was used to measure load-line displacement (LLD), shown in Fig. 2.10. The specimen was then installed in the test fixture, and a careful inspection was performed to confirm that the load-contact points mated properly. Figure 2.11 shows CB-1.1 in the test fixture in preparation for the fatigue precracking phase. Figure 2.12 illustrates the test specimen, loading fixture, and the load transfer configuration.

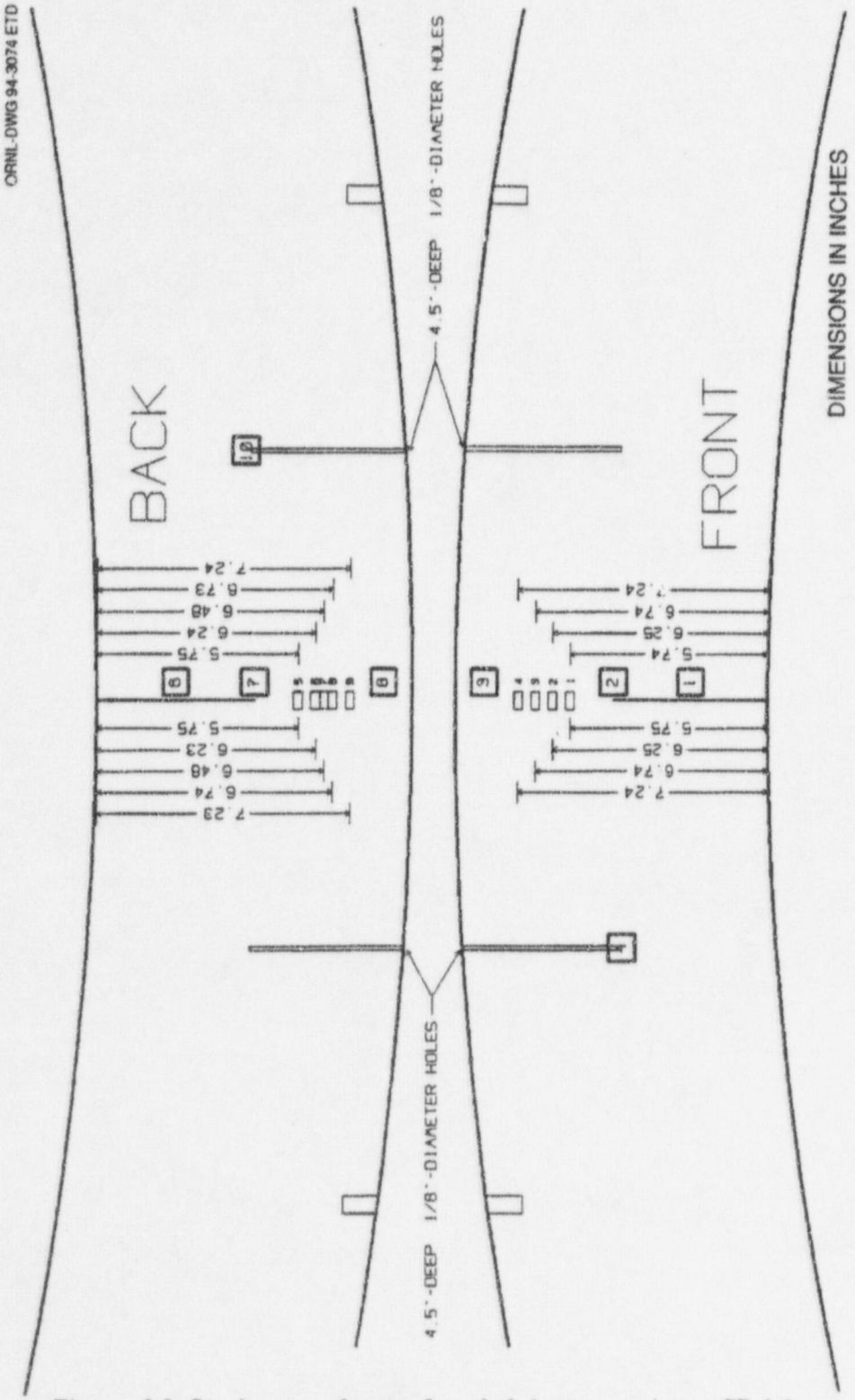

Figure 2.9 Strain gage layout for clad beam specimen CB-1.1.

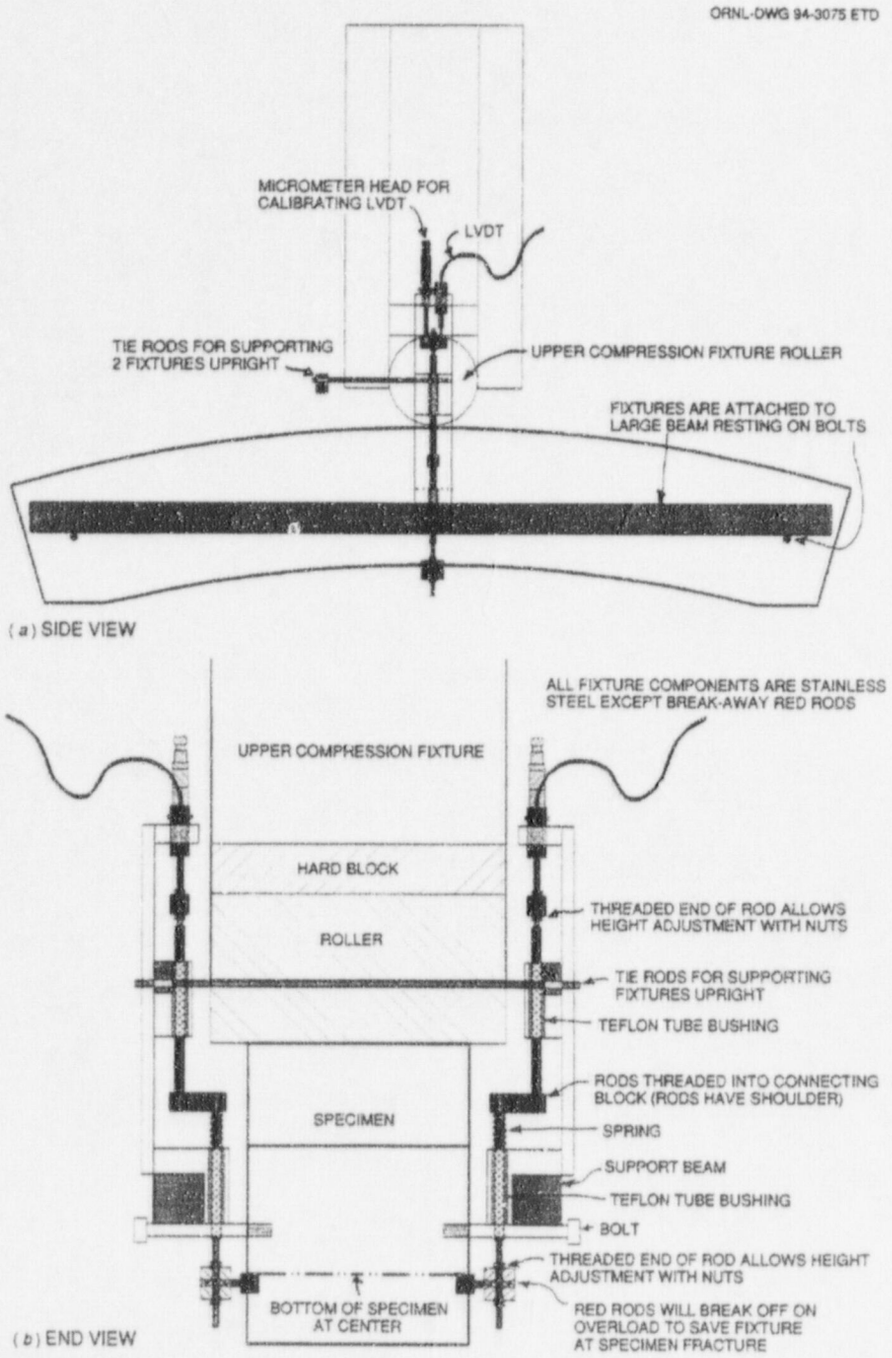

Figure 2.10 **Fixture used to measure load-line displacement (LLD) on clad beam tests: (a) side view and (b) end view.**

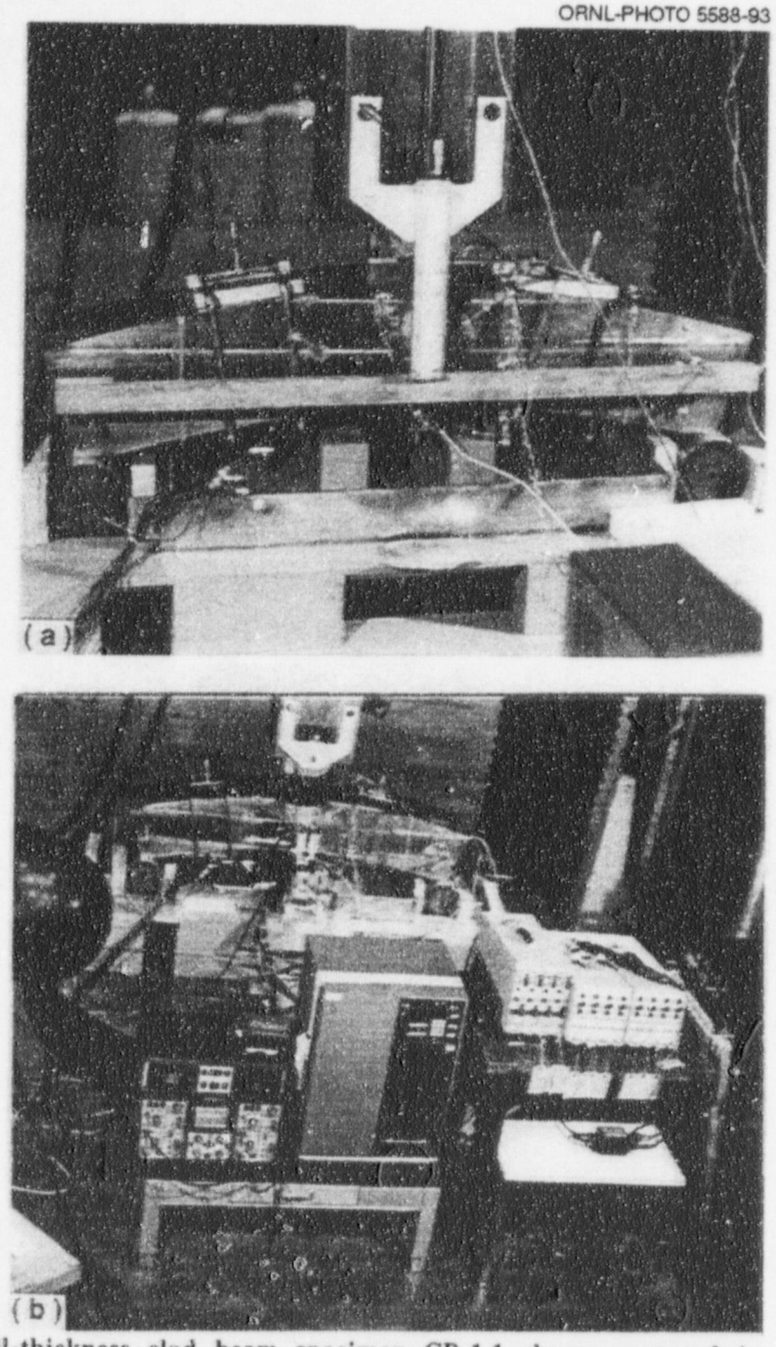

Figure 2.11 (a) **Full-thickness clad beam specimen CB-1.1 shown mounted in test fixture during fatigue precracking and (b) data collection equipment shown in relative positions.**

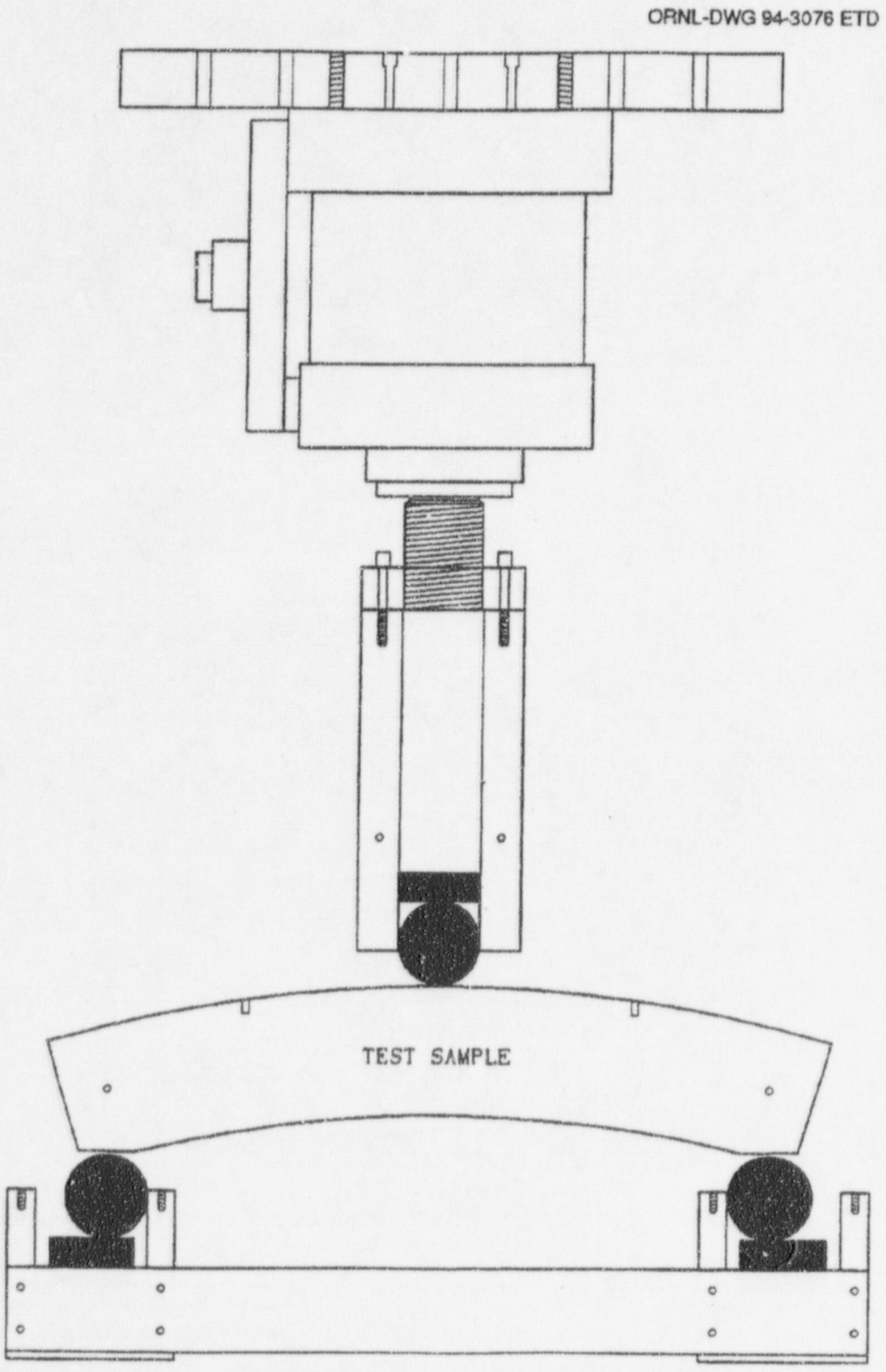

Figure 2.12 Schematic of load system and test beam.

For the fracture phase, the manifold for spraying the LN_2 onto the beam surface was mounted around the specimen, and the environmental chamber was used to enclose the assembly. Figure 2.13 shows a test beam mounted in the loading fixture, with the LN_2 manifold in place, but with the load-line displacement (LLD) instrumentation and the environmental chamber not yet installed. Once the specimen was completely enclosed, it was cooled to the test temperature (-25 °C) per the procedures just discussed. The specimen was then loaded to fracture under stroke control using a constant displacement rate. The same failure test procedure and the same general instrumentation layout was used for all specimens.

The fracture surface for specimen CB-1.4 is shown in Fig. 2.14. The fracture surface can be divided into three parts. The lower part is the machined flaw surface, where the uniformity, or straightness, of the crack front is clearly visible. The second part is the crack-growth produced during fatigue precracking. The third part is the fracture surface itself, which shows a cleavage fracture. While there are multiple initiation sites, the first initiation location appeared to be near the center of the crack front. Note that, with the exception of portions of the crack front near the beam sides, the flaw growth was very uniform. The fracture surface for specimen CB-1.5 is shown in Fig. 2.15. During the CB-1.5 test, a violent failure of the beam resulted in one half of the specimen and two rollers being ejected from the test fixture. The test fixture was significantly damaged by this action. Based on load vs deflection data, substantial plasticity developed in the beam before failure. Examination of the fracture surface revealed that the fatigue crack was followed by approximately 2.6 mm of ductile tearing and then by a fairly flat cleavage surface.

2.3 Test Results

Applied load (P) vs displacement curves for each of the five beams are shown in Fig. 2.16 for LLD and in Fig. 2.17 for CMOD, respectively. These curves depict the inelastic behavior in the shallow-crack specimens as fracture conditions are approached. In contrast, near-elastic conditions are demonstrated for deep-crack specimen CB-1.1. The conditions of each specimen at failure are listed in Table 2.3.

Table 2.3 Summary of test results from the full-thickness clad beam testing program

	CB-1.1	CB-1.2	CB-1.3	CB-1.4	CB-1.5
a/W	0.50	0.05	0.10	0.10	0.05
Temperature, °C*	-25.5	-25.0	-25.0	-25.3	-25.9
Stroke Rate**, mm/min	2.49	8.38	6.89	3.76	8.76
Time to Failure, s	230	366	440	309	556
Failure conditions					
P, kN	1232.5	5002.3	5060	3114	5783
LLD, mm	3.236	5.767	8.083	2.825	16.396
CMOD, mm	1.485	0.567	1.718	0.318	1.998

*Temperature values vary by ± 1°C

**Stroke (load) rate was selected to give comparable $\dot{K}$ for each flaw configuration.

ORNL-PHOTO 8317-92

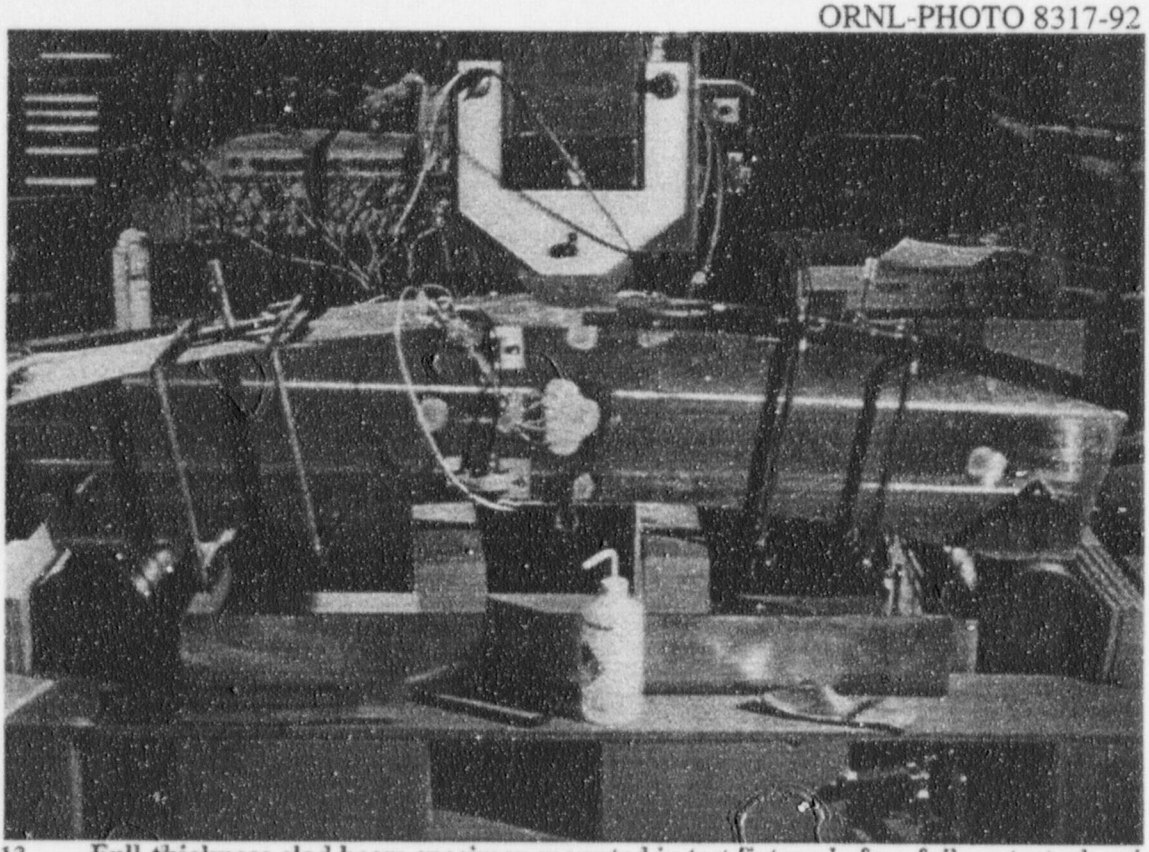

Figure 2.13 **Full-thickness clad beam specimen mounted in test fixture before failure test, showing LN_2 manifold in place.**

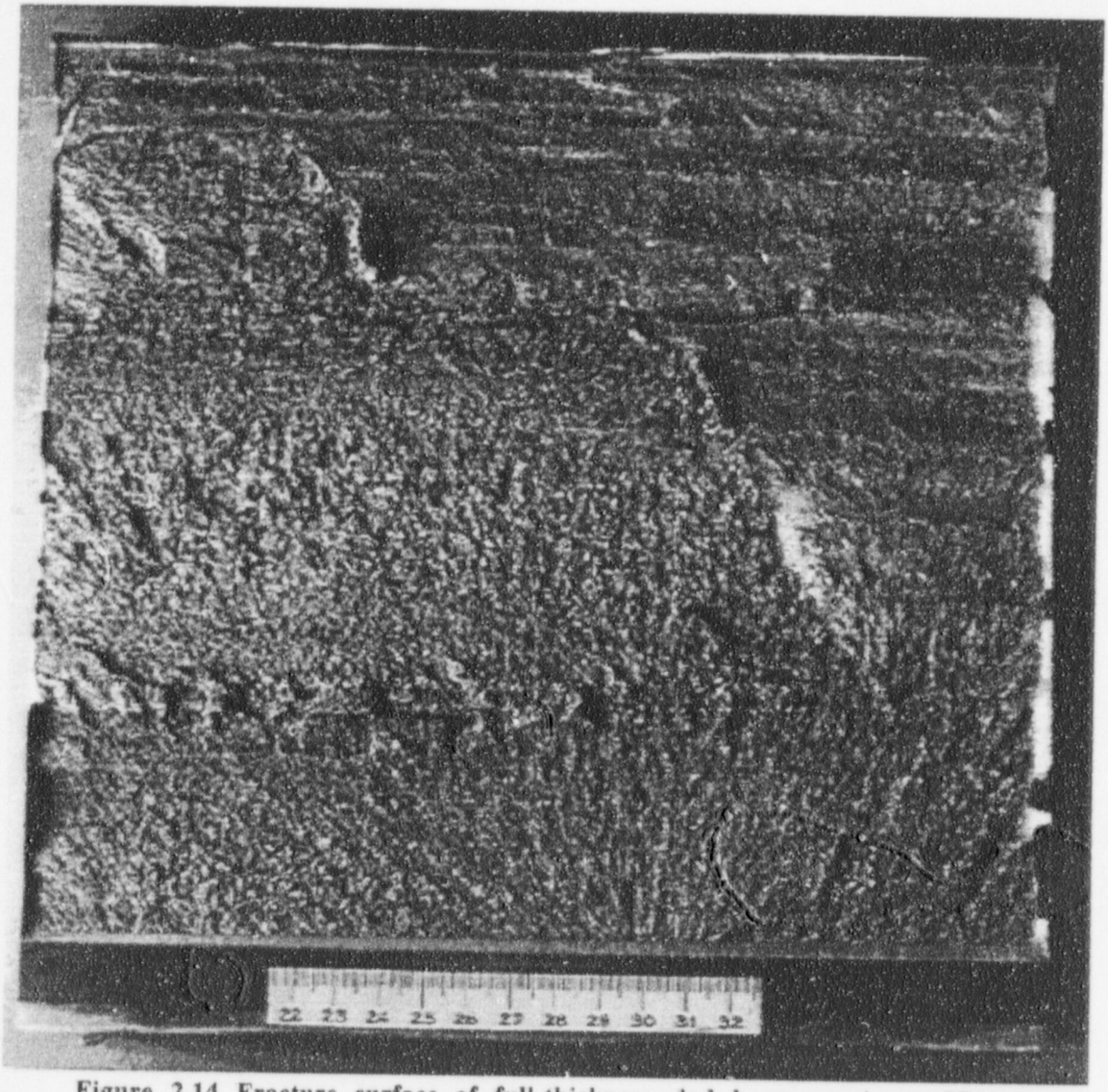

Figure 2.14 Fracture surface of full-thickness clad beam specimen CB-1.4

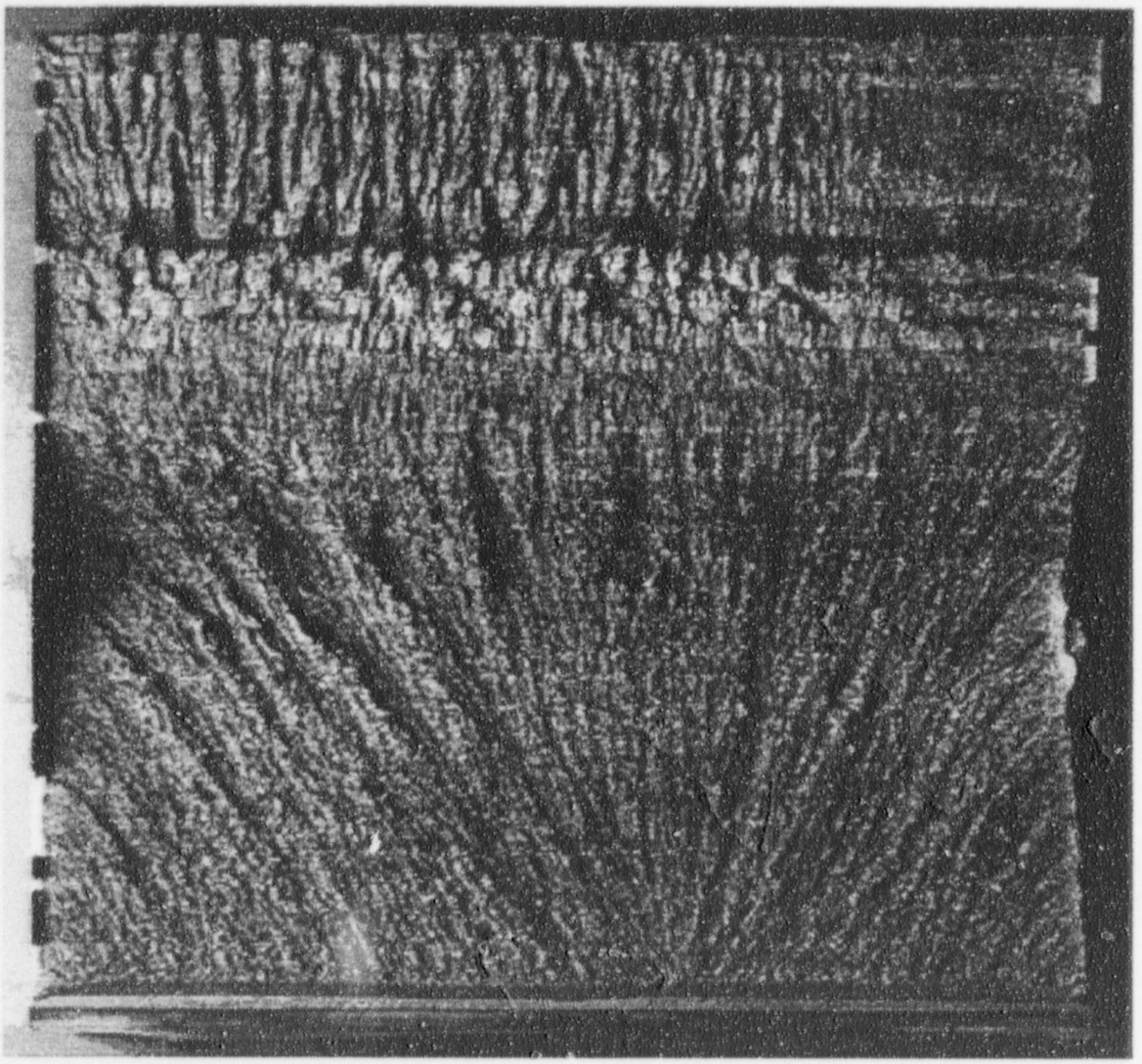

Figure 2.15 Fracture surface of full-thickness clad beam specimen CB-1.5

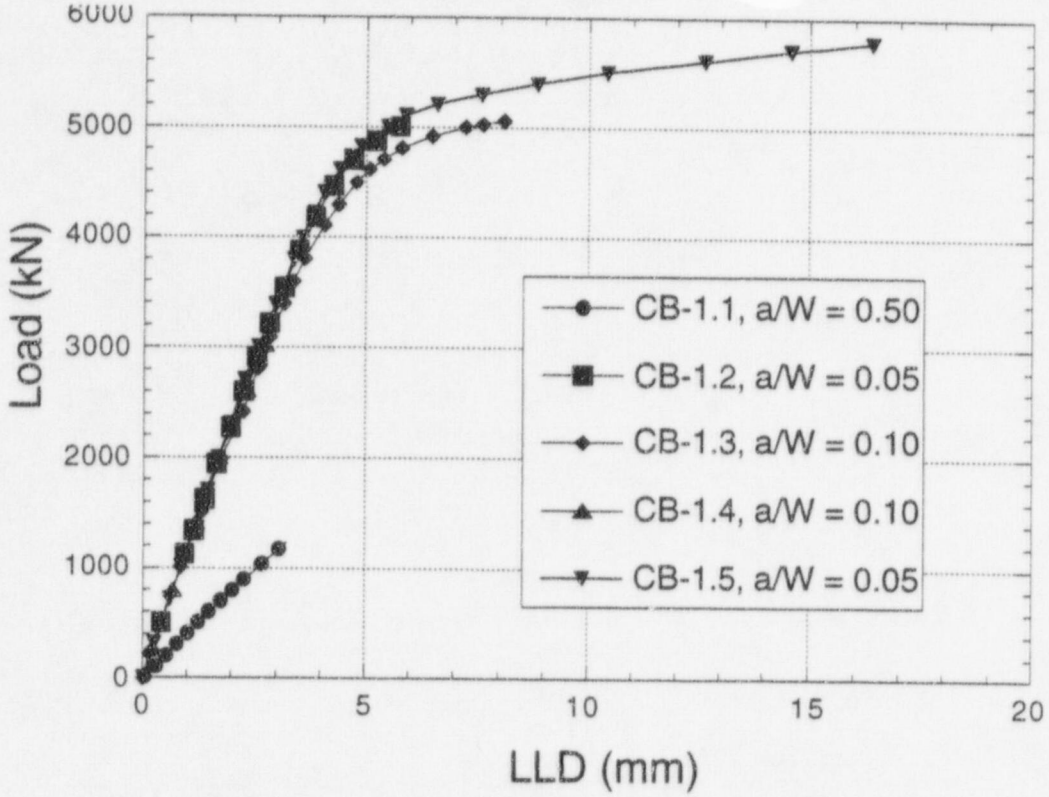

Figure 2.16 Load vs LLD for CB-1.1, 1.2, 1.3, 1.4, and 1.5

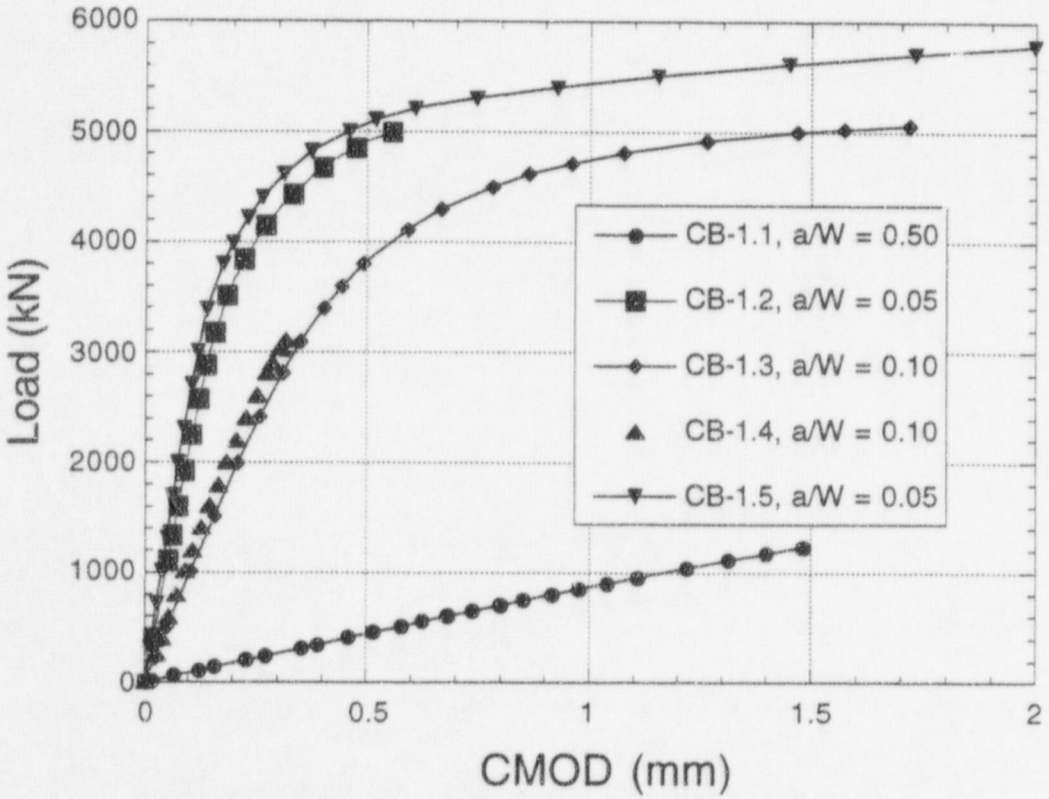

Figure 2.17 Load vs CMOD for CB-1.1, 1.2, 1.3, 1.4, and 1.5

3 Clad Beam Posttest Analyses

3.1 Finite-Element Analysis Models

Two analytical techniques were used to generate finite-element solutions for the full-thickness clad beams. In clad beam tests CB-1.1 through CB-1.4, the crack initiated in cleavage, thus allowing use of static analysis techniques.[12] The CB-1.5 specimen experienced approximately 2.6 mm of stable ductile tearing before initiation of cleavage fracture. Recent studies indicate that the onset of stable ductile tearing leads to crack-tip profiles and crack-tip fields ahead of the growing crack that differ from those of a stationary crack. Stable ductile tearing exposes additional volumes of material to elevated near-crack-tip fields as the crack advances, thus altering the sampling of potential cleavage initiation sites on the microstructural level. Also, measured cleavage fracture toughness values for these specimens are influenced by changes in crack-tip constraint conditions that occur with prior stable crack growth. The analysis of CB-1.5 utilized the Gurson-Tvergaard (G-T) dilatant plasticity model[13] for void growth and element extinction, providing the capability to simulate crack growth. This methodology is described in detail in Appendix A.

3.1.1 Cleavage Model

A two-dimensional (2-D) analysis was performed on the clad beam specimen CB-1.4 depicted in Fig. 2.5 using the ABAQUS[14] finite-element program (analyses of CB-1.1 through CB-1.3 are described in detail in Ref. 11). A one-half section of the complete clad beam specimen illustrated in Fig. 2.5 is represented in the 2-D finite-element model of Fig. 3.1. This model of the clad beam specimen ($a/W = 0.10$) incorporates the curvature of the plate and the flat region where the specimen is supported during loading.

A highly refined mesh in the crack-tip region (see Fig. 3.1c) provides resolution of stress fields over the normalized distance $2 < r / (J / \sigma_0) < 10$ in front of the crack; where r is the distance from the crack tip, and σ_0 is the yield stress. The outermost semicircular ring of nodes in the mesh, shown in Fig. 3.1c, has a radius of 3.6 mm.

The model consists of 3630 nodes and 1105 eight-node isoparametric elements with a reduced 2×2 Gaussian quadrature. Collapsed-prism elements arranged in a focused-fan configuration at the crack tip are used to produce an approximate $1/r$ strain singularity appropriate for inelastic analysis. A distributed-pressure is used to load the model over four elements on the outer edge (see Fig. 3.1b).

Plane-strain analyses were carried out using an incremental elastic-plastic constitutive model (von Mises) and small-strain theory. Local crack-tip fields obtained from these analyses were applied in stress-based dual-parameter characterization models to assess constraint effects.

3.1.2 Precleavage Ductile Tearing Model

The finite-element model shown in Fig. 3.2 was employed to perform plane-strain nonlinear analyses of the clad beam specimen CB-1.5 ($a/W = 0.05$) which had a small amount of precleavage ductile tearing (~2.6 mm). The finite-element computer code WARP3D[15] (see Appendix A for details) was used to perform the analysis. WARP3D was developed at the University of Illinois as a research tool in the field of fracture mechanics with specific features oriented toward the investigation of ductile fracture in metals. With the Gurson-Tvergaard (G-T) model, void nucleation and growth ahead of a stably tearing crack are incorporated into a finite-element model with computational cells having explicit length scales, as illustrated in Fig. 3.3. For 2-D plane-strain analyses, the WARP3D code utilizes a one-element-layer thick 3-D model; plane-strain constraints are imposed on all nodes.

In Fig. 3.2, the mesh has 2706 nodes and 1248 elements. Symmetry about the crack plane permits modeling of one-half of the specimen. Square elements in the crack-tip region and along the crack plane are defined to permit uniform increments of crack extension. The crack-tip element size is 100 μm (chosen from prior analytical experience[16]) for adequate resolution of the crack-opening profile and stresses ahead of the growing crack. The finite-element model is loaded by displacement increments imposed on six centerplane nodes (the two end elements) as shown in Fig. 3.2a.

The Gurson constitutive formulation is used for the elements along the crack plane where ductile tearing occurs, and the remaining material is modeled by the von Mises yield criterion with associated flow rule. Two principal input parameters for the G-T model are the initial void volume fraction, f_0, and the characteristic length, D, associated with the G-T crack plane elements. According to theory, these parameters are dependent only on the material and not on specimen geometry. At the time that the plane-strain analyses were carried out no experimental $J - \Delta a$ curves for the weld material were available;

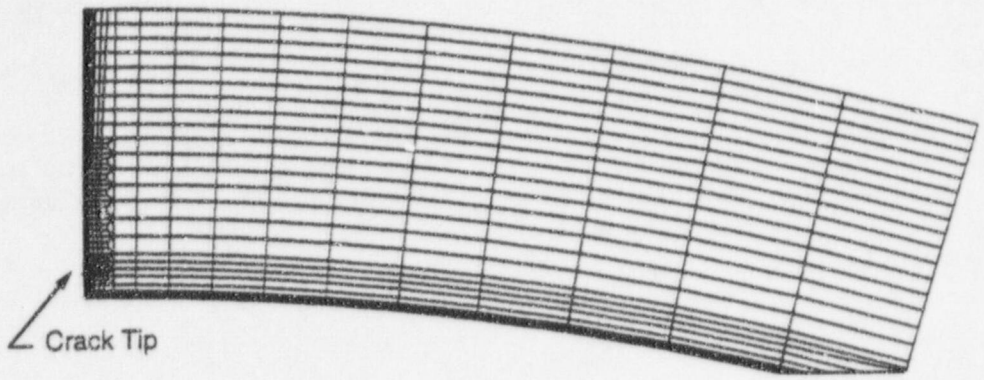

(a)

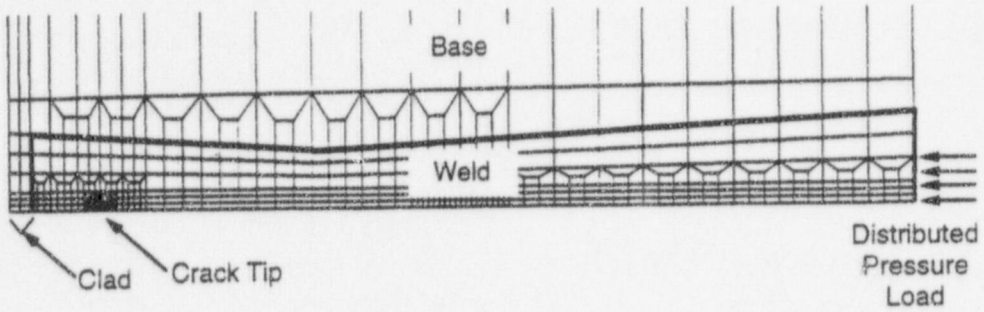

(b)

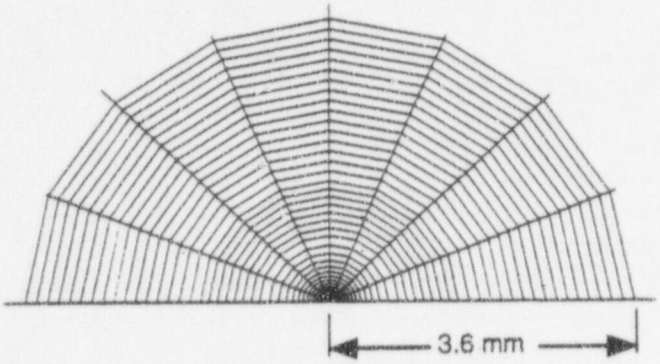

(c)

Fig. 3.1 **(a) Finite-element mesh of clad beam specimen CB-1.4 (a/W=0.10), (b) crack-plane region, and (c) crack-tip region.**

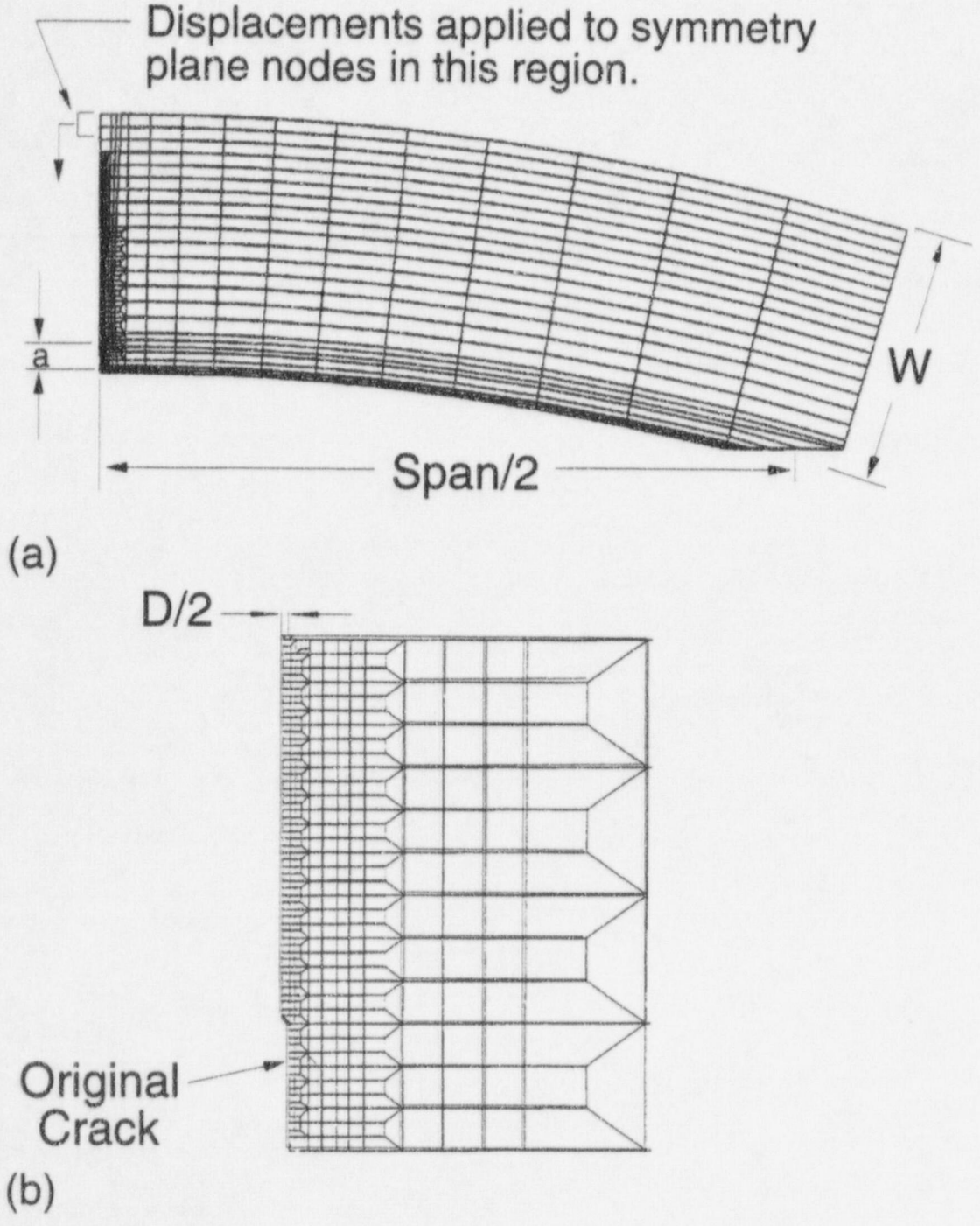

Fig. 3.2 **(a) Finite-element mesh of clad beam specimen CB-1.5 (a/W=0.05), (b) crack-plane region.**

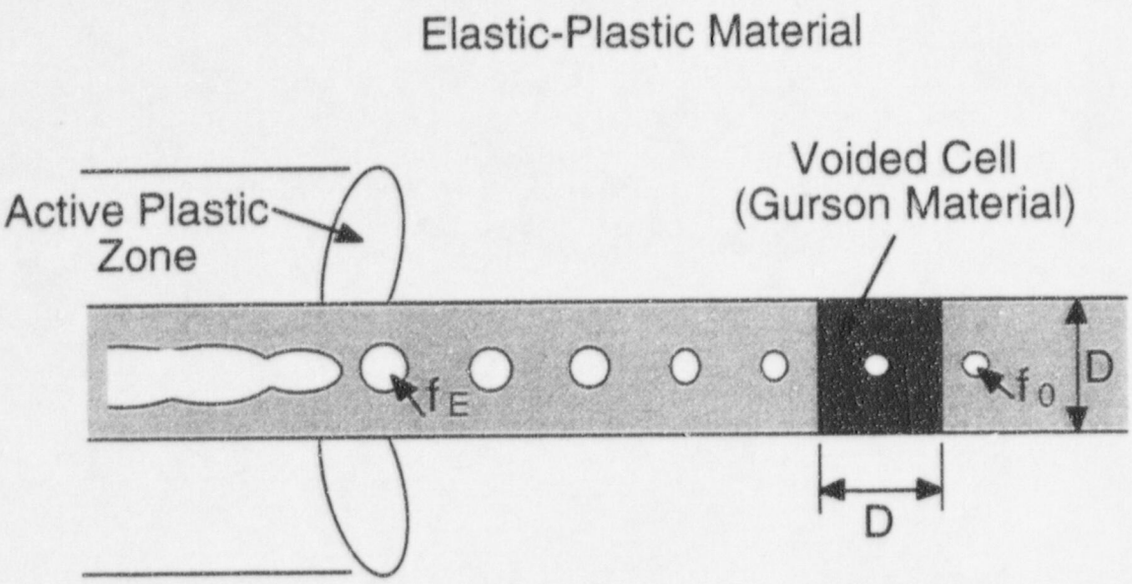

Figure 3.3 Two material damage parameters for the Gurson-Tvergaard model: initial slab height D and initial volume fraction f_0

there, a parametric study was performed to obtain the initial volume fraction f_0 and displacement increment which would reproduce the experimental load vs CMOD curve for CB-1.5. The value of f_0 used in the final analysis was 0.006 with a displacement increment of 0.00215. The explicit length scale D was set at 200 μm (since the crack-tip element size is 100 μm). Upon the void fraction f increasing to the critical volume fraction, set at $f_f = 0.15$, void coalescence occurs. Full interpretation of the test results from CB-1.5 has not been completed. Additional work is on-going as noted later in the report.

Material properties used for the posttest analyses of the clad beam specimens were taken from Table 2.2 and from the true stress vs true plastic strain curves given in Fig. 3.4.

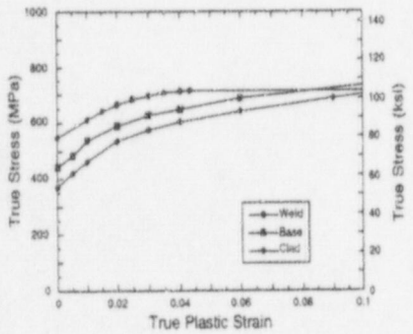

Figure 3.4 Material representation for clad beam.

3.2 Calibration of the G-T Model

Two principal input parameters for the G-T model are the initial void volume fraction, f_0, and the characteristic length, D, associated with the G-T crack plane elements. According to theory, these parameters are dependent only on the material and not on specimen geometry. To evaluate this model, the steps illustrated in Fig. 3.5 were taken:

- Ductile crack growth data were generated from side-grooved compact tension (CT) specimens taken from the weld material.
- The parameters f_0 and D were selected for the material to get agreement with load versus CMOD and crack growth data from the CT specimens.
- The same values of these parameters from the CT specimen analyses were then used to analyze the full-thickness clad beams using a 3-D model to determine if they predict the observed responses.

Calibration analyses were performed with the WARP3D fracture analysis computer program[15] which incorporates the Gurson-Tvergaard (G-T) dilatant plasticity model for void growth and an element extinction capability for

modeling crack growth. Two principal input parameters for the G-T model are the initial void volume fraction, f_0, and the characteristic length, D, associated with the G-T crack plane elements. Ductile crack growth data were generated from side-grooved CT specimens taken from the RPV weld and base material. The parameters f_0 and D were calibrated for the weld and base material through an iterative process involving finite-element analyses of the CT specimens. A three-dimensional (3-D) model for a 1T CT specimen (20% side grooved and $a/W = 0.63$, depicted in Fig. 3.6) was used for the calibration analyses.

For the weld material, calibration analyses were carried out for a D of 254 mm, f_C of 0.15, and values for q_1, q_2, and q_3 of 1.25, 1.0, and 1.5625, respectively. The q values were introduced by Tvergaard in the equation for the G-T yield condition to improve the model predictions for periodic arrays of cylindrical and spherical voids. A value of 0.002 for f_0 gave the best approximation to the experimental load P vs LLD and J vs Δa curves.

For the base material, a value of 0.0008 for f_0 gave the best approximation to the experimental load vs LLD and J vs Δa curves (for the same D and f_C values as the weld material). The values of q_1 and q_2 were adjusted to 1.35 and 0.95, respectively, due to the particular strain hardening of this material.

The calculated values for J vs Δa, shown in Fig. 3.7, are close to measured values for the CT tests [SNB02 and SNB04 (Base material); SNL02 and SNL04 (Weld material)]. Figure 3.8 shows the measured final crack profiles for the CT test specimens, which are in good agreement with the numerical models (also shown in Fig. 3.8). Note that reverse tunneling near the side grooves is visible in the CT specimens (base material) and predicted in the analysis.

3.3 Analytical Results

Results from the *a posterior* plane-strain analyses of tests CB-1.4 and CB-1.5 are summarized in Figs. 3.9 and 3.10. Comparison of the measured and calculated P vs displacement responses provides an interpretation of the accuracy of the analysis results and a means of establishing confidence in the calculated fracture mechanics parameters.

The calculated P vs LLD curves are compared with measured data for each test in Fig. 3.9. For comparison, results for test CB-1.1, CB-1.2, and CB-1.3 are also included in Fig. 3.9. Calculated LLD values at a given load for the shallow-crack specimens were greater than the measured values for the full range of loading, except CB-1.5 where the measured values of LLD are greater than the calculated values over the plastic range of loading.

Comparisons of calculated and measured P vs CMOD in Fig. 3.10 show good agreement for CB-1.1 through -1.4. To match the measured CMOD at failure for CB-1.5, the load had to be increased by 12 %, because the plane-strain model was too stiff.

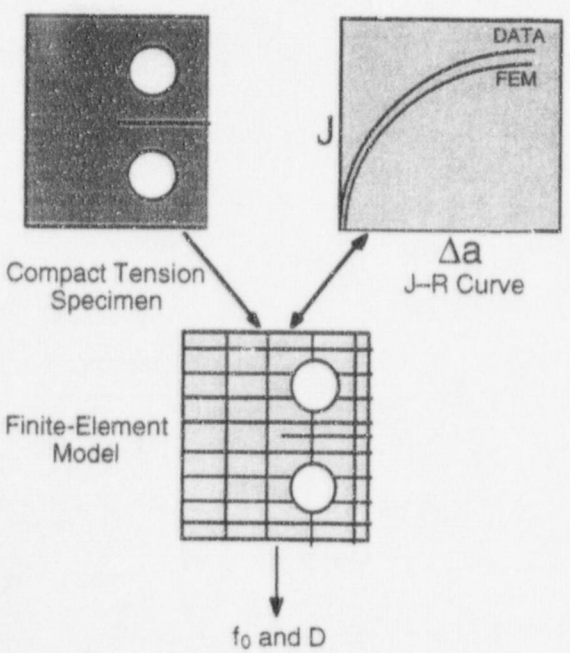

Figure 3.5 Calibration of Gurson model parameters f_0 and D using small laboratory specimens

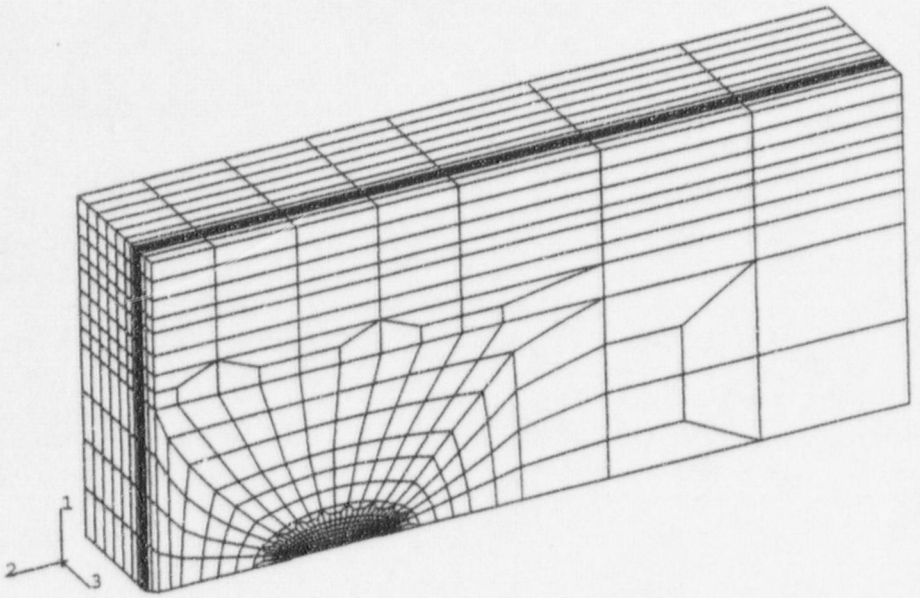

(a)

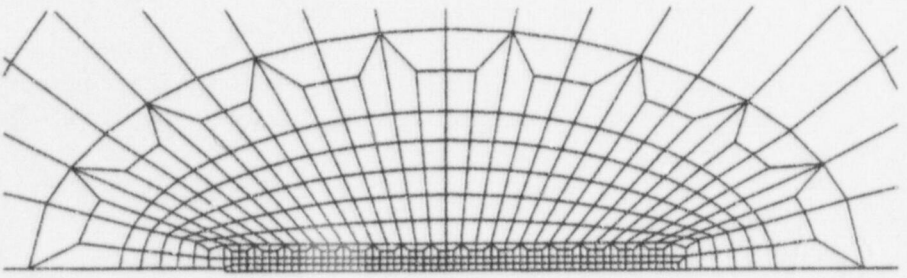

(b)

Figure 3.6 **Three-dimensional finite-element model of 1T-CT specimen: (a) complete mesh, and (b) crack-plane region.**

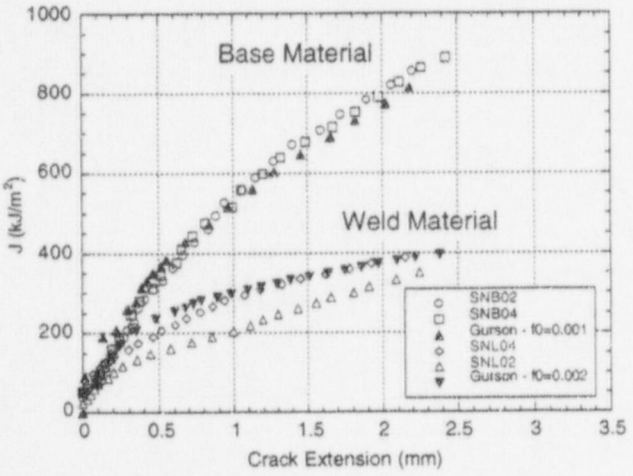

Figure 3.7 **Comparison of calculated and measured crack extension for specimens fabricated from the SNUPPs weld and base material.**

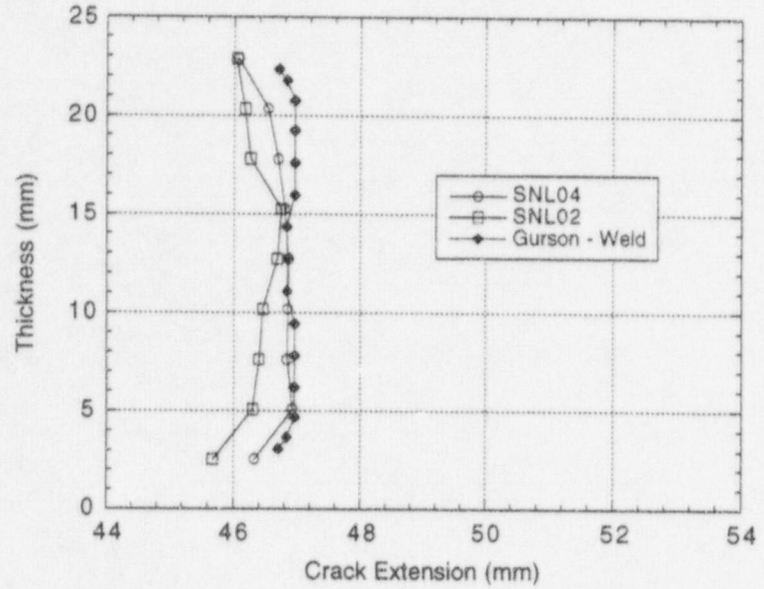

(a)

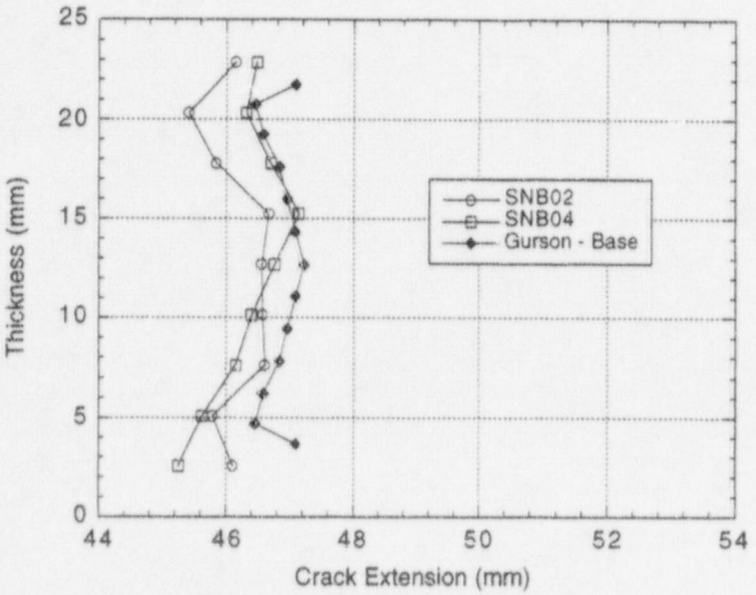

(b)

Figure 3.8 Comparison of calculated and measured final crack front shape for specimens fabricated from the SNUPPs material: (a) weld and (b) base.

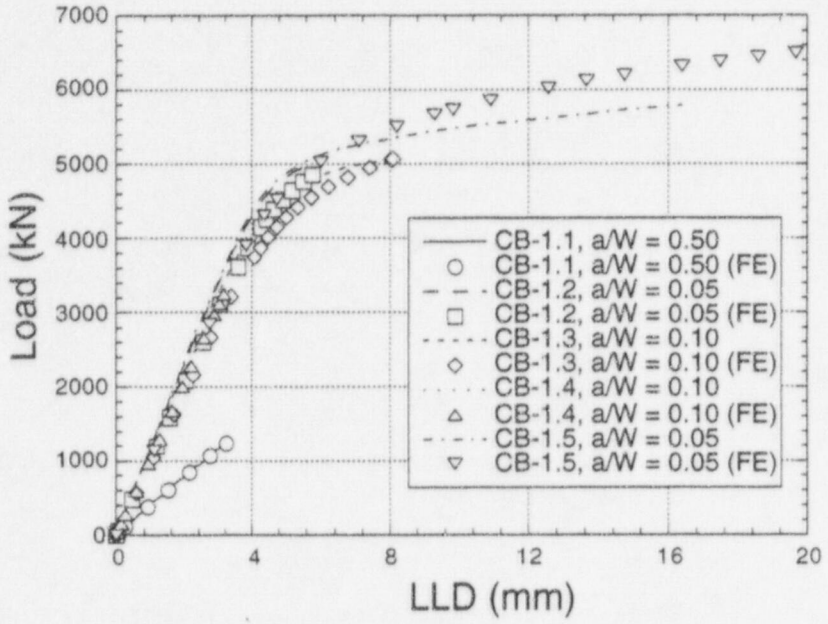

Figure 3.9 Comparison of calculated (plane strain model) and measured LLD for clad beam specimens

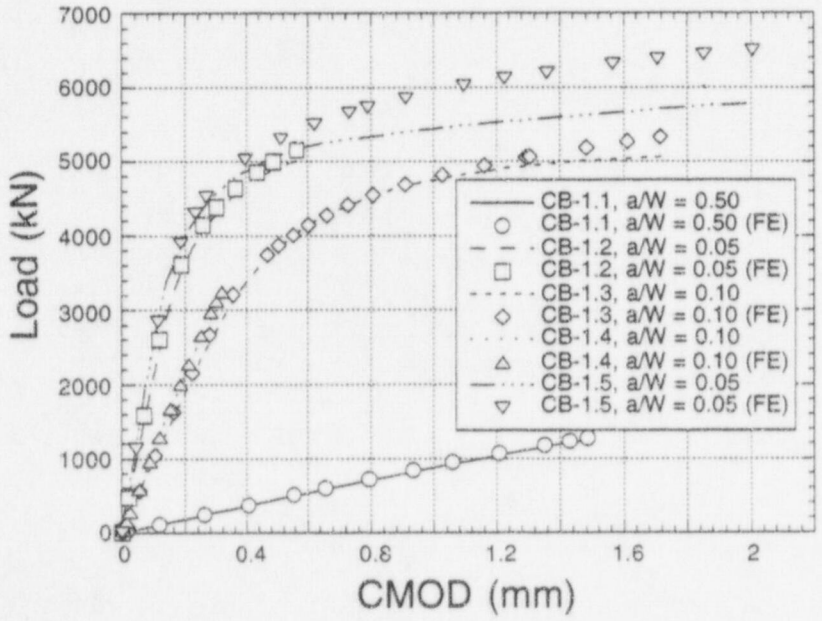

Figure 3.10 Comparison of calculated (plane strain model) and measured CMOD for clad beam specimens.

Table 3.1 Summary of analysis results from the full-thickness clad beam testing program

	CB-1.1	CB-1.2	CB-1.3	CB-1.4	CB-1.5
a/W	0.50	0.05	0.10	0.10	0.05
U_{pl}, kN-mm	135	6427	16879	93	—[a]
A_{pl}, kN-mm	88	1473	5486	79	—[a]
η-factors					
η_{pl}^{ℓ}	1.37	0.79	1.05	1.69	—
η_{pl}^{c}	2.26	4.16	4.08	2.82	—
Fracture toughness					
Elastic component					
J_{el}, kJ/m^2	131.3	110.6	230.5	73.52	151.6[b]
K_I, MPa$\sqrt{\text{m}}$	173.0	154.5	223.1	126.0	180.9
P vs CMOD					
J_{pl}, kJ/m^2	8.1	124.7	486.0	4.69	—
Total J, kJ/m^2	139.4	235.3	716.5	78.21	1082.5[c]
K_{Jc}, MPa$\sqrt{\text{m}}$	173.5	225.4	393.3	130.0	483.5
P vs LLD					
J_{pl}, kJ/m^2	7.4	103.8	384.8	3.31	—
Total J, kJ/m^2	138.7	214.4	615.3	76.83	—
K_{Jc}, MPa$\sqrt{\text{m}}$	173.1	215.2	364.5	128.8	—

[a]Not calculated since CB-1.5 underwent precleavage ductile tearing and toughness was not estimated using η-factors.

[b]Static analysis for crack depth location after ductile tearing (a ~ 14.7 mm).

[c]Gurson-Tvergaard plasticity model for void growth and element extinction for crack growth.

The plane strain model results for CB-1.5, shown in Figs. 3.11 and 3.12 and given in Table 3.1, indicate that the crack began tearing at a load of 5659 kN (J value of 373 kN/m). The crack extended 2.6 mm with an end load of 6497 kN and J value of 1083 kN/m. The difficulties in analytically modeling the measured responses of P vs LLD and P vs CMOD simultaneously have been described in previous reports.[4, 11-12, 17] For the analyses presented herein, emphasis was placed on modeling the P vs CMOD response accurately for use in determining fracture toughness.

A three-dimensional model of the full-thickness clad-beam specimen was generated using the mesh-generator code PATRAN. The finite-element model is shown in Fig. 3.13. Values of the weld calibrated parameters for the CT specimen analyses(see Sect. 3.1.3) were transferred to the clad-beam model (CB-1.5) to determine if they predict the response observed in the test. Comparisons of calculated and measured load (P) vs CMOD in Fig. 3.14 shows good agreement for CB-1.5 (tests CB-1.1 – CB-1.4 are also included). The 3-D model results of CB-1.5, shown in Fig. 3.15, indicate that the crack began tearing at a load of 4400 kN (J value of 94 kJ/m^2). The crack extended to 2.6 mm (the amount of tearing in the test) at a load of 5600 kN (J value of 880 kJ/m^2), which is close to the measured cleavage fracture load in the experiment (5780 kN).

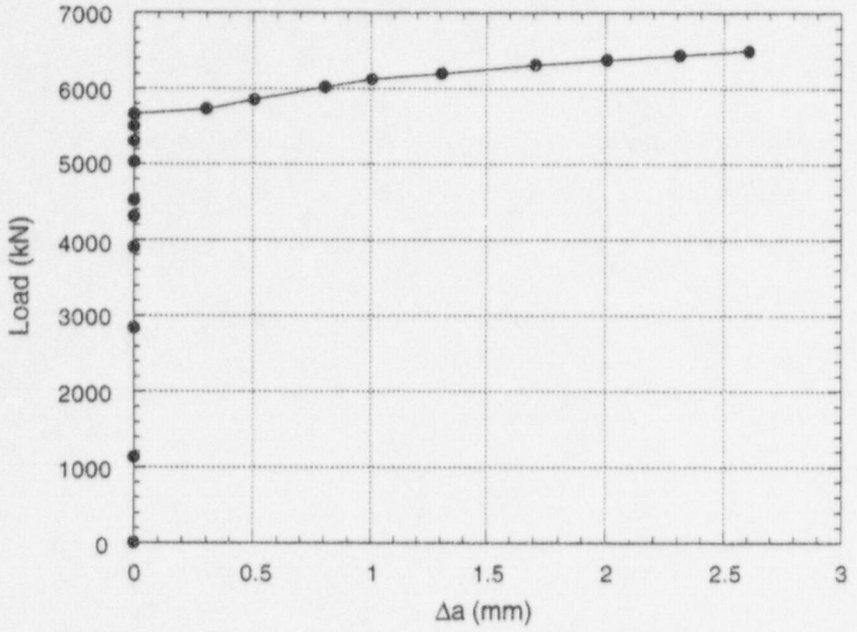

Figure 3.11 Plane strain model results for clad beam specimen CB-1.5 – P vs Δa.

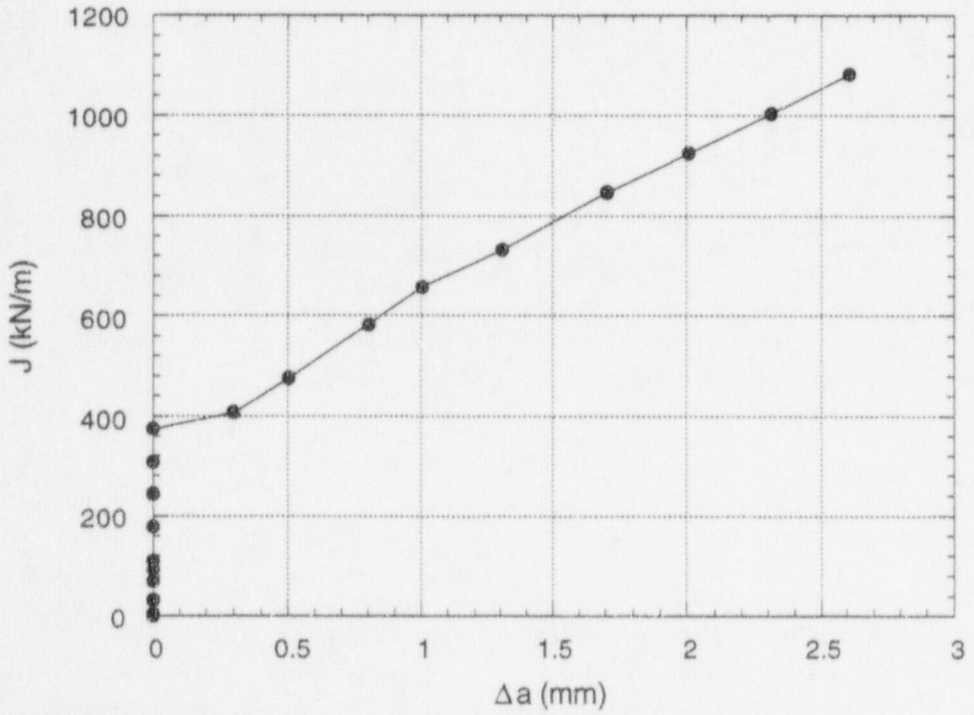

Figure 3.12 Plane strain model results for clad beam specimen CB-1.5 – J vs Δa.

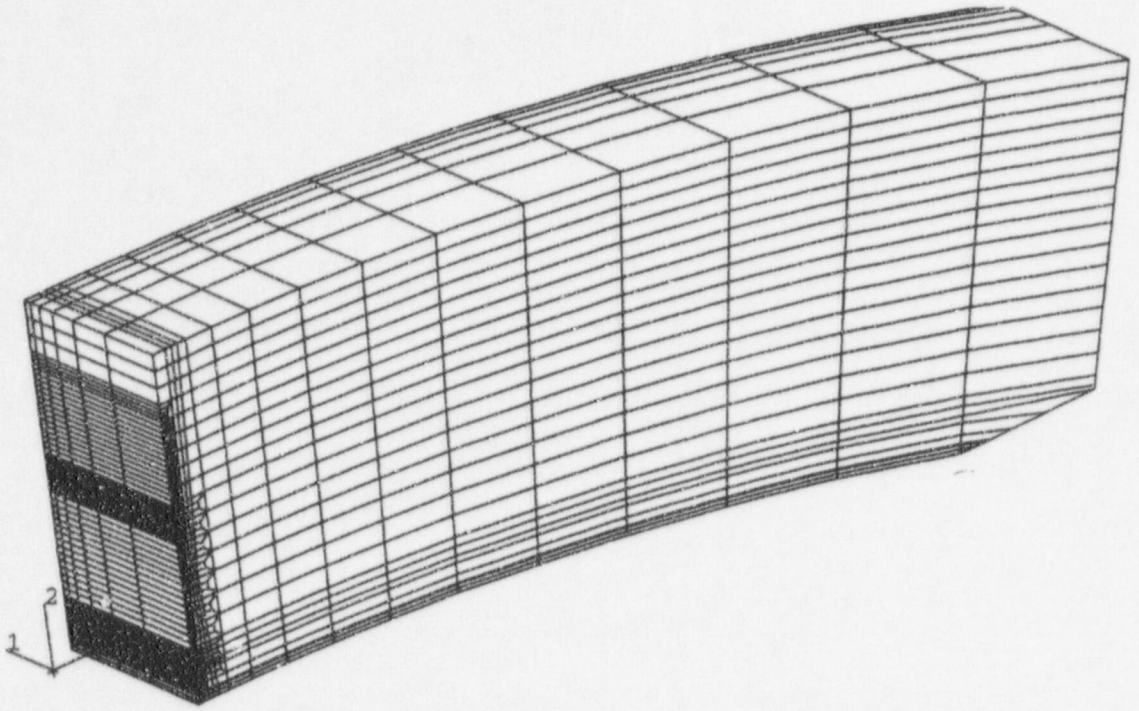

Figure 3.13 Three-dimensional finite-element model of the clad beam specimen CB-1.5

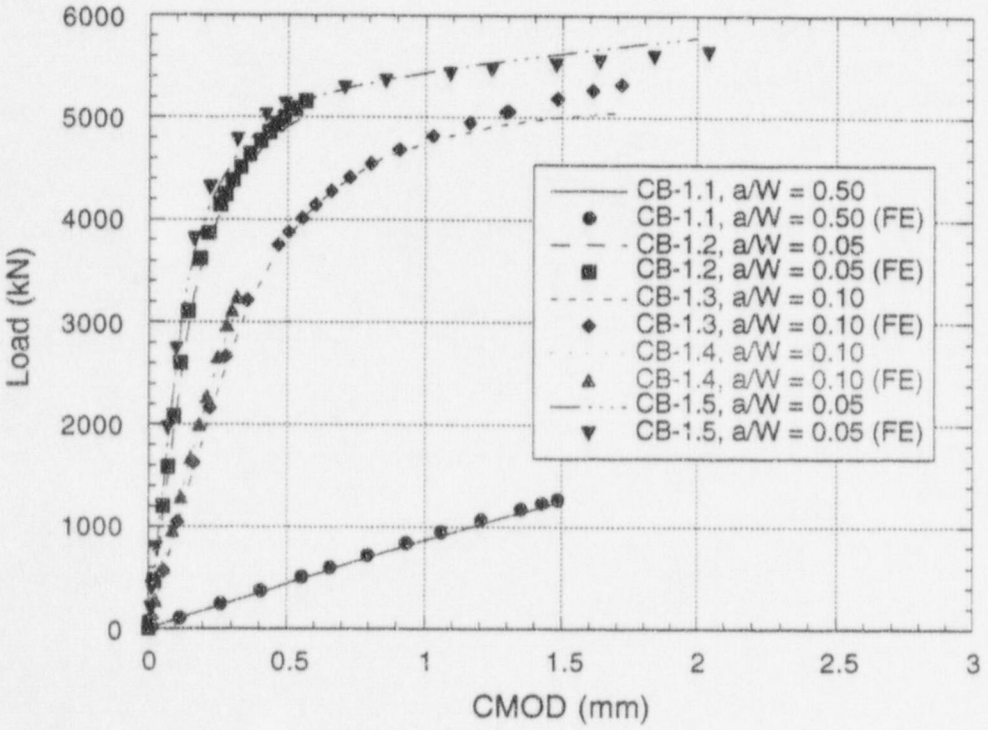

Figure 3.14 Calculated (3D model) and measured displacement for the clad-beam specimens.

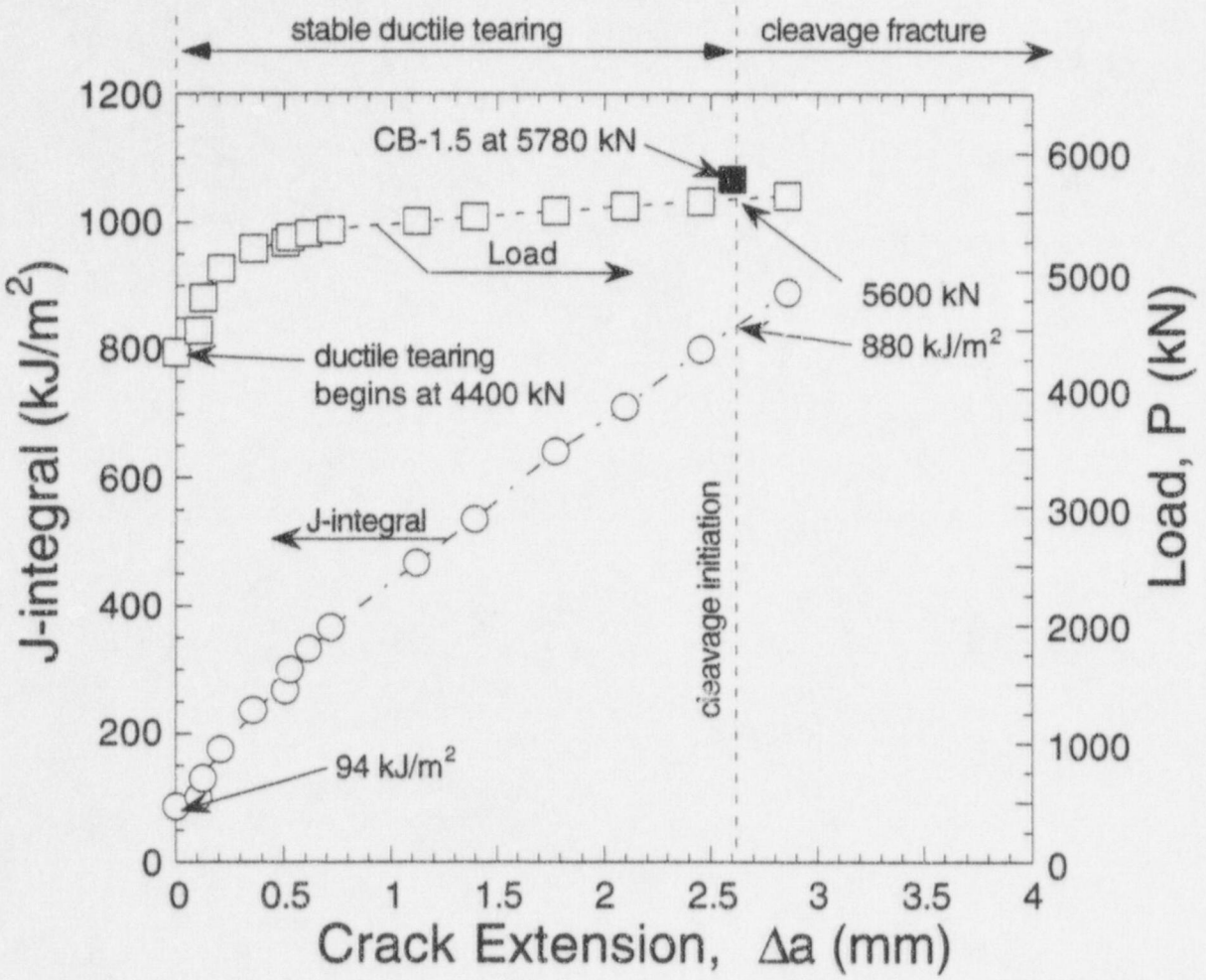

Figure 3.15 Three-dimensional model results for clad-beam specimen CB-1.5: P vs Δa and J vs Δa

3.4 Toughness Estimation Techniques

For the clad beam tests, fracture toughness is estimated in terms of the critical J-integral and then converted into an elastic-plastic stress-intensity factor, K_{JC}. The two techniques[4,11-12,17] used to determine the critical J for CB-1.1 through CB-1.4 (cleavage initiation) are based on the "work" at the crack tip as measured by the area under the load–displacement (LLD or CMOD) curves. The methods require an η-factor, which relates work at the crack tip to the plastic portion of the crack-driving force. The first method of estimating J uses the P vs LLD test record as input for the toughness estimate. The J-integral is divided into elastic and plastic parts given by

$$J = J_{el} + J_{pl} \tag{3.1}$$

where

$$J_{pl} = \frac{\eta_{pl}{}^{l} U_{pl}}{Bb} \ . \tag{3.2}$$

and U_{pl} is the plastic component of the area under the P vs LLD curve, B is the specimen thickness, b is the remaining ligament (W-a), and $\eta_{pl}{}^{l}$ is the dimensionless constant relating the area term to J_{pl}. Finite-element analysis provides values of $\eta_{pl}{}^{l}$ as a function of U_{pl} for each loading and specimen configuration. Analysis is also required to determine the relationship between J_{el} and P. The U_{pl} value from the measured P vs LLD curve and the corresponding value of $\eta_{pl}{}^{l}$ for each test at cleavage initiation are included in Table 3.1. The second technique[18] for determining the critical J-integral uses the plastic component of the area under the P vs CMOD curve (A_{pl}) to calculate J_{pl}. The values of A_{pl} (from the measured P vs CMOD data) and $\eta_{pl}{}^{l}$ for each test at initiation are listed in Table 3.1. Cleavage fracture toughness values for the full-thickness clad beams are given in Table 3.1.

In Fig. 3.16, values of J calculated for CB-1.4 from the two η-factor techniques are compared to J determined from finite-element analyses. These results showed relatively good agreement among the three methods of calculating J.

3.5 Residual Stresses

An analytical study was carried out to estimate the effects of residual stresses on measured cleavage fracture toughness data obtained from the full-thickness clad beam specimens CB-1.1 through CB-1.4. A thermal gradient method (TGM) was used to generate stress distributions in the beams that approximate the residual stresses. These estimates of stress distribution were based on previous residual-stress studies[19] conducted at ORNL. In the latter studies, the TGM was based on application of a temperature distribution in the form of a cosine function through the thickness of the beam. The temperature distribution was adjusted such that the generated stresses in the beam would cause the opening displacements of a pre-crack notch in the beam to match those recorded during the wire electro-discharge machining of the notch. These fictitious thermal stresses were then imposed as initial stresses on each of the clad beam models containing fatigued through-flaws. It should be noted that residual stress values may be larger in the RPV shell segment from which the clad beam specimens were fabricated. A previous study[20] has shown that the stress level in a specimen cut from a plate is lower than the stress level in the uncut plate, because the stresses in the specimen were allowed to relax when the restraining effects of the plate were removed.

Estimates of residual stress effects on cleavage fracture toughness values measured in each of the four tests are summarized in Table 3.2. Contributions of the residual stresses to the K-factor applied to the fatigue-sharpened flaw (with no externally applied load) are given in Column 1 of Table 3.2. Columns 2 and 3 provide estimates of fracture toughness based on CMOD η-factors (Table 3.1) that exclude and include the effects of residual stresses, respectively. Residual stresses were shown to have a measurable effect only on the shallow-crack toughness data.

Fracture toughness data from the HSST clad beam and shallow-crack single-edge-notched bend (SENB) programs[4] are shown in Fig. 3.17 as a function of normalized temperature (T-NDT). Figure 3.17 indicates an increase in mean toughness and data scatter with decreased constraint associated with shallow crack testing in the transition temperature region. The range in scatter for data obtained from the clad beam specimens is consistent with that from the laboratory-scale SENB specimens tested at the same temperature. Note that the minimum toughness value from the clad beam specimens was provided by a shallow-crack beam, not by the single deep-cracked beam tested in this series.

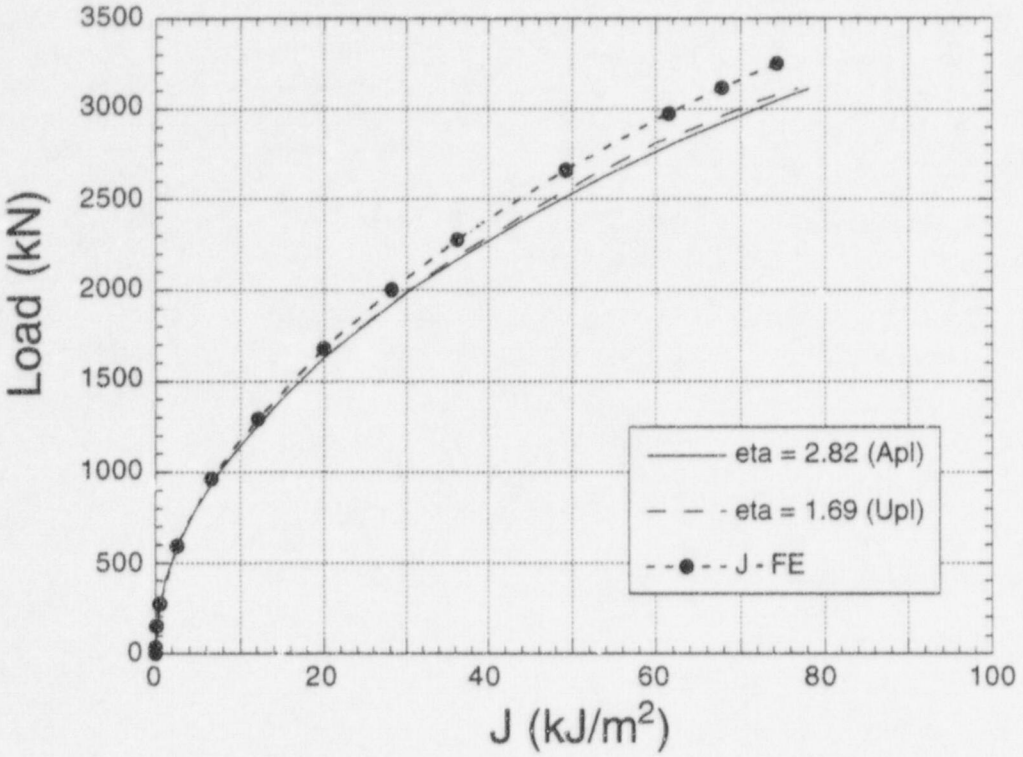

Figure 3.16 **Comparison of calculated (plane strain model) J values for full thickness clad beam specimen CB-1.4 (a/W = 0.10)**

Table 3.2 Summary of residual stress results from the full-thickness clad beam testing program.

Test	a/W	K (MPa$\sqrt{m}$) (1) Residual Stress (RS)	(2) Without RS (η -factors)	(3) With RS (η -factors)
CB-1.1	0.50	6	174	174
CB-1.2	0.05	18	225	243
CB-1.3	0.10	24	393	411
CB-1.4	0.10	24	130	155

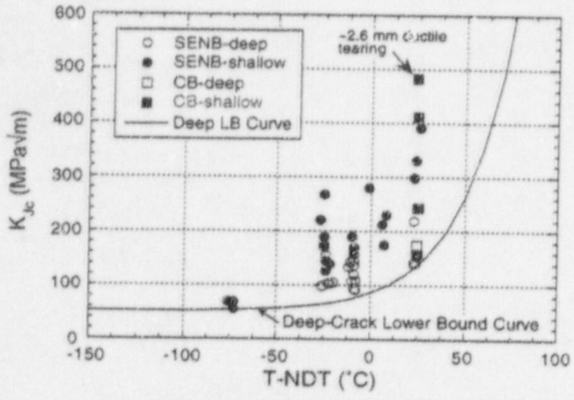

Figure 3.17 Fracture toughness as function of normalized temperature *T – NDT*.

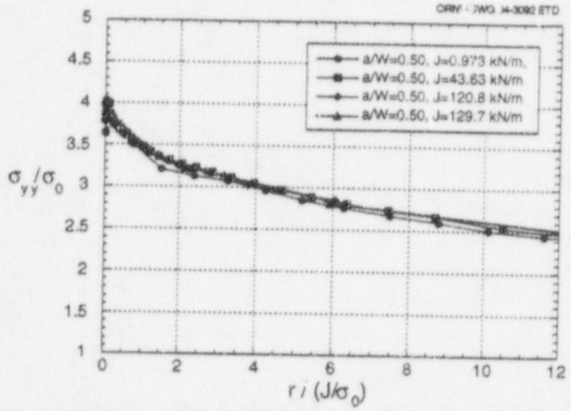

Figure 3.18 Distributions of normalized opening-mode stress for deep-crack clad beam specimen as a function of applied *J* up to crack initiation.

3.6 Constraint Analyses

The dual-parameter stress-based *J-Q* methodology[6-8] was used to assess crack-tip stress triaxiality in the clad beam specimens that experienced cleavage initiation.[1] In these analyses, results for the deep-crack specimen (CB-1.1) at a *J* value of 43.63 kJ/m² (J_c = 139.4 kJ/m² in Table 2.3) are employed as an approximation to the small-scale yielding (SSY) reference solution. Earlier analyses[4] have shown that Q is approximately zero for the deep-crack specimens under these loading conditions. This observation is supported by results shown in Fig. 3.18 for the normalized opening-mode stress (σ_{yy}/σ_0) distributions vs $r / (J / \sigma_0)$ for the deep-crack specimen CB-1.1.

The opening-mode stresses ahead of the crack tip for the shallow-crack specimen (CB-1.4), shown in Fig. 3.19, exhibit an essentially uniform deviation from the SSY solution over a distance of $2 < r/(J/\sigma_0) < 10$ (i.e., spatially uniform). From Fig. 3.19, the clad beam specimen CB-1.4 has a *Q*-stress value of about –0.36 at failure (for $2 < r / (J / \sigma_0) < 10$), whereas CB-1.2 and CB-1.3 had *Q*-stress values of –0.78 at failure (a significant loss of constraint). This moderate loss of constraint in the CB-1.4 specimen is due primarily to the relatively lower failure load observed in the test.

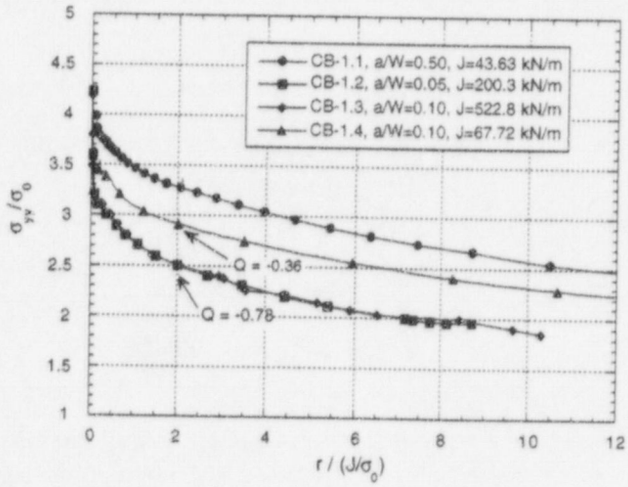

Figure 3.19 Distributions of normalized opening-mode stress for clad beam specimens as a function of applied *J*: *a/W* = 0.50, 0.05, and 0.10.

4 Summary and Conclusions

This report describes results from an HSST testing program that is utilizing full-thickness clad beam specimens fabricated using material from the RPV of a canceled nuclear power plant. The beam specimens, which incorporate RPV fabrication weld, base, and clad overlay materials, are providing fracture toughness data for shallow cracks in material for which metallurgical conditions are prototypic of those found in RPVs. Factors influencing the fracture toughness of RPV material containing shallow cracks include material property gradients, weld inhomogeneities, the cladding process, and residual stresses.

In the first testing phase, five full-thickness clad beam specimens were fabricated with through-thickness cracks that ranged in depth from 10 to 114 mm ($0.05 \le a/W \le 0.5$) in the weld material. These specimens were tested in three-point bending at temperatures in the transition region of the weld metal fracture toughness curve ($T - NDT$ about 25 °C). Fracture toughness estimates were obtained from P vs LLD and P vs CMOD data using finite-element techniques and estimation schemes based on the η-factor method. The inclusion of residual stress estimates had a measurable effect on the shallow-crack toughness data.

The cleavage toughness data were compared with other shallow- and deep-crack uniaxial beam data generated previously from base material that conformed to SA533, Grade B requirements. The range in scatter for data obtained from the clad beam specimens is consistent with that from the laboratory-scale SENB specimens tested at the same temperature. The minimum toughness value from the clad beam specimens was provided by a shallow-crack beam, not by the single deep-cracked beam tested in this series.

These data should be regarded as preliminary, because the potential effects of material property gradients in the HAZ (associated with the cladding) were not considered in the toughness determinations. Material testing is currently underway to provide updated material property data for the base, weld, clad, and clad HAZ.

In the HSST Program, initial studies of ductile tearing models have focused on the Gurson-Tvergaard (G-T) dilatant plasticity model for void growth and an element extinction capability for modeling crack growth. Two principal input parameters for the G-T model are the initial void volume fraction, f_0, and the characteristic length, D, associated with the G-T crack plane elements. According to theory, these parameters are dependent only on the material and not on specimen geometry. To evaluate this model, ductile crack growth data were generated from side-grooved CT specimens taken from the weld material. The parameters f_0 and D were then calibrated for the material through an iterative process involving finite-element analyses of these CT specimens (see Fig. 3.5). The calibrated parameters provided analytical results in agreement with load versus CMOD and crack growth data from the CT specimens. Values of these parameters from the CT specimen analyses were transferred to a 3-D model of the full-thickness clad beams. Comparisons of calculated and measured load (P) vs CMOD showed good agreement for CB-1.5. Analytical results of CB-1.5 also indicated that the crack began tearing at a load of 4400 kN (J value of 94 kN/m). The crack extended to 2.6 mm (the amount of tearing in the test) at a load of 5600 kN (J value of 880 kN/m), which is close to the measured cleavage fracture load in the experiment (5780 kN).

Additional full-thickness clad beam tests have been tested and results are being evaluated to complete the investigation of fracture toughness of shallow cracks located in prototypical full-thickness plate material. Shallow-crack fracture toughness results from these specimens should provide additional data that are essential to a better understanding of the effects of metallurgical conditions in the region of the clad HAZ.

References

1. W. Marshall et al., "An Assessment of the Integrity of PWR Pressure Vessels," United Kingdom Atomic Energy Agency Study Group Reports, March 1982.*

2. U. S. Nuclear Regulatory Commission Regul? Guide 1.154, "Format and Content of Plant-Specific Pressurized Thermal Shock Safety Analysis Reports for Pressurized Water Reactors," January 1987.†

3. R. D. Cheverton and D. G. Ball, Martin Marietta Energy Systems, Inc., Oak Ridge Natl. Lab., "Pressurized-Thermal-Shock Evaluation of the Calvert Cliffs Nuclear Power Plant," pp. 201-244, USNRC Report NUREG/CR-4022 (ORNL/TM-9408), September 1985.‡

4. T. J. Theiss, D. K. M. Shum, and S. T. Rolfe, Martin Marietta Energy Systems, Inc., Oak Ridge Natl. Lab., "Experimental and Analytical Investigation of the Shallow-Flaw Effect in Reactor Pressure Vessels," USNRC Report NUREG/CR-5886 (ORNL/TM-12115), July 1992.‡

5. *The American Society of Mechanical Engineers Boiler and Pressure Vessel Code*, Section XI, "Rules for Inservice Inspection of Nuclear Power Plant Components," Appendix A, "Analysis of Flaws," Article A-4000, Material Properties, American Society of Mechanical Engineers, New York, 1998.†

6. N. P. O'Dowd and C. F. Shih, "Family of Crack-Tip Fields Characterized by a Triaxiality Parameter: Part I—Structure of Fields," *J. Mech. Phys. Solids* **39**, 989–1015 (1991).§

7. N. P. O'Dowd and C. F. Shih, "Family of Crack-tip Fields Characterized by a Triaxiality Parameter: Part II—Fracture Applications," *J. Mech. Phys. Solids* **40**, 939–963 (1992).§

8. N. P. O'Dowd and C. F. Shih, Naval Surface Warfare Center, "Two Parameter Fracture Mechanics: Theory and Applications," USNRC Report NUREG/CR-5958 (CDNSWC/SME-CR-16-92), February 1993.‡

9. F. M. Haggag, "In-Situ Measurements of Mechanical Properties Using Novel Automated Ball Indentation System," pp. 27–44 in *Small Specimen Test Techniques Applied to Nuclear Reactor Vessel Thermal Annealing and Plant Life Extension, ASTM STP 1023*, W. R. Corwin, F. M. Haggag, and W. L. Server, eds., American Society for Testing and Materials, 1993.‡

10. *American Society of Mechanical Engineers Boiler and Pressure Vessel Code*, Section III, "Rules for Construction of Nuclear Power Plant Components," American Society of Mechanical Engineers, New York, 1989.§

11. J. A. Keeney et al., Martin Marietta Energy Systems, Inc., Oak Ridge Natl. Lab., "Preliminary Assessment of the Fracture Behavior of Weld Material in Full-Thickness Clad Beams," USNRC Report NUREG/CR-6228 (ORNL/TM-12735), October 1994.‡

12. T. J. Theiss et al., Martin Marietta Energy Systems, Inc., Oak Ridge Natl. Lab., "Initial Results of the Influence of Biaxial Loading on Fracture Toughness," USNRC Report NUREG/CR-6036 (ORNL/TM-12349), June 1993.‡

13. A. L. Gurson, "Continuum Theory of Ductile Rupture by Void Nucleation and Growth: Part I — Yield Criteria and Flow Rules for Porous Ductile Media," *J. Engng. Mater. Tech.* **99**, 2-15 (1977).§

14. *ABAQUS Theory Manual*, Version 5–2, (Hibbit, Karlson, and Sorensen, Inc., Providence, R. I., 1992).**

15. K. C. Koppenhoefer, A. S. Gullerud, C. Ruggieri, R. H. Dodds, Jr., and B. E. Healy, Department of Civil Engineering, University of Illinois, "WARP3D: Dynamic Nonlinear Analysis of Solids Using a Preconditioned Conjugate Gradient Software Architecture," UILU-ENG-94-2017, November 1994.

16. C. Ruggieri and R. H. Dodds, Jr., "A Transferability Model for Brittle Fracture including Constraint and Ductile Tearing Effects: A Probabilistic Approach," *Int. J. Fract.* **79**, 309-340 (1996).§

17. B. R. Bass et al., Martin Marietta Energy Systems, Inc., Oak Ridge Natl. Lab., "Biaxial Loading and Shallow-Flaw Effects on Crack-Tip Constraint and Fracture Toughness," USNRC Report NUREG/CR-6132 (ORNL/TM-12498), January 1994.‡

18. M. T. Kirk and R. H. Dodds, Jr., Department of Civil Engineering, University of Illinois, "*J* and CTOD Estimation Equations for Shallow Cracks in Single Edge Notch Bend Specimens," USNRC Report NUREG/CR-5969 (CDNSWC/SME-CR-17-92), July 1993.

19. J. A. Keeney, Martin Marietta Energy Systems, Inc., Oak Ridge Natl. Lab., "Residual Stress Analysis of Full-Thickness Clad Beam Specimens," (ORNL/NRC/LTR-94/37), August 14, 1995.

20. E. F. Rybicki, J. R. Shadley, and A. S. Sandhu, The University of Tulsa, Mechanical Engineering Associates, Inc., "Experimental Evaluation of Residual Stresses in a Weld Clad Plate and Clad Test Specimens," NUREG/CR-4646, MEA-2145, October 1986.

21. W. J. McAfee, B. R. Bass, J. W. Bryson, Jr., and W. E. Pennell, Martin Marietta Energy Systems, Inc., Oak Ridge Natl. Lab., "Biaxial Loading Effects on Fracture Toughness of Reactor Pressure Vessel Steel," NUREG/CR-6273 (ORNL/TM-12866), March 1995.

---

*Available in NRC Public Document Room for inspection and copying for a fee.

†Copies are available from U.S. Government Printing Office, Washington, D.C. 20402. ATTN: Regulatory Guide Account.

‡Available for purchase from the National Technical Information Service, Springfield, VA 22161.

§Available from public technical libraries.

**Available for purchase from organization sponsoring the cited publication, and/or from authors, and/or recipients.

Appendix A

Ductile Tearing Model Development

In recent years, developments of models to quantify ductile tearing resistance in steels increasingly have emphasized the coupling of fracture processes on the microscale with conventional continuum approaches. Particular attention has been given to constitutive models that describe the evolution of local damage in front of the growing crack. Constraint conditions that influence triaxiality of the crack-tip stress fields also affect the extent of plastic flow around the crack-tip. Higher stress triaxiality inhibits plastic flow, promotes void growth on the micromechanical level, and leads to increased damage in the fracture process zone. Constitutive equations have been formulated to describe the physical effects of constraint on void nucleation, growth and coalescence and, consequently, on tearing resistance. An advantage claimed for micromechanical models over conventional continuum models is that material parameters describing the tearing process can be transferred in a more general way among different specimen geometries. Typically, these parameters for the damage model are determined through a process which combines small-specimen testing and numerical modeling.

A.1 Gurson Model

The Gurson formulation[A1] is comprised of a yield condition, flow rule, definition of void volume fraction, criteria for void nucleation, and a rule for evolution of the void volume fraction. Microvoids nucleate at inclusions and second-phase particles by a process of debonding or cracking during plastic deformation. The ratio of the void volume to the whole volume of a unit cell is defined as the void volume fraction (f). The temporal evolution of f is governed by two terms that define void nucleation and growth rates,

$$\dot{f} = \dot{f}_{growth} + \dot{f}_{nucleation} \quad , \tag{A.1}$$

where the growth rate is given by

$$\dot{f}_{growth} = (1-f)D_{kk}^{\ p} \quad , \tag{A.2}$$

and the initial condition by

$$f(t_0) = f_0 \quad . \tag{A.3}$$

Here D_{ij} denotes components of the symmetric part of the spatial velocity gradient tensor and $D_{ij}^{\ p}$ the plastic part thereof.

To describe the nucleation of voids, Brocks et al.[A2] adopt the empirical formulation of Needleman and Rice,[A3]

$$\dot{f}_{nucleation} = A\dot{\sigma}_m + (B/3)\dot{\sigma}_{kk} \quad , \tag{A.4}$$

where σ_{ij} is the macroscopic Cauchy stress. Brocks et al.[A2] reference the formulation of Chu and Needleman[A4] for the parameters A and B. These parameters have one form if void nucleation is driven by accumulated plastic strain (strain controlled), or another form if controlled by hydrostatic stress (stress controlled).

In the material matrix undergoing plastic deformation, the nucleated micro-voids experience shape changes and volumetric growth. Gurson[A1] used a relationship which postulates that void growth rate depends exponentially on the stress triaxiality to describe plastic yielding of a matrix material containing voids. The constitutive relation employed to model an elastic-plastic solid containing voids is a form of the Gurson model as modified by Tvergaard and Needleman.[A5-A8] The central feature of the modified Gurson model is the yield function given by

$$\Phi = (\sigma_e/\sigma_0)^2 + 2q_1 f \cosh\left((3q_2\sigma_m)/(2\sigma_0)\right) - \left(1+q_3 f^2\right) = 0 \quad . \tag{A.5}$$

Here, σ_e is the macroscopic Mises effective stress, σ_m the macroscopic mean stress, σ_0 the current flow stress, f the current void volume fraction, and q_1, q_2, q_3 are factors proposed by Tvergaard.[A8] (Typical values for these factors are $q_1 = 1.25$, $q_2 = 1.0$, and $q_3 = q_1^2$). A flow law relating the plastic strain rate to the stress rate is provided in various references (for example, see Refs. A2 and A9). For the void-free condition given by $f = 0$, the Gurson model reduces to the J_2 incremental flow theory of plasticity.

A modified form of the void volume fraction (f^*) is employed to account for coalescence of voids which occurs after a critical volume fraction (f_C) is reached:

$$f^* = \begin{cases} f & \text{for } f \le f_c \\ f_c + K(f - f_c) & \text{for } f > f_c \end{cases} \qquad \text{with } K = \frac{f_u^* - f_c}{f_f - f_c} \,. \tag{A.6}$$

The material loses stress-carrying capacity when the final void volume fraction (f_f) is reached, and where f^* achieves its ultimate value f_u^*.

The modified Gurson formulation has been augmented with equations to account for strain rate and temperature dependence of the current yield stress.[A10] Also, this model has been combined with an adiabatic heating model to incorporate the effects of temperature increase due to plastic work in dynamic fracture analyses.[A11-A12] Two groups of material parameters are required to characterize this model:

- parameters associated with classical rate independent plasticity or strain-rate dependent plasticity, which would include temperature effects, and
- parameters required for the modified Gurson model, i.e., ε_n, f_n, s_n, f_0, f_c, f_f, and q_1, q_2, q_3.

Three parameters, i.e., ε_n, f_n, s_n, are required to model void nucleation [through Eq. (A.4)], while other parameters, i.e., f_0, f_c, and f_f describe void growth, coalescence, and failure.

Strategies for evaluating the parameters in the modified Gurson model are discussed by Brocks et al.[A2] Even though there may not be a generally accepted scheme for determining these parameters, load vs reduction of diameter curves from notched tensile bars appear to provide one avenue. Values for the parameters f_0, f_c, and f_f are determined by fitting various segments of the computationally determined load vs reduction in diameter curve with the experimental data. It should be noted that the void volume fraction, f_0, was not determined from micrographs of the material. Tensile bars from a mild steel with notch radii of 4 mm and 10 mm were used to characterize parameters in the modified Gurson model as follows: $f_0 = 0.0025$, $f_c = 0.021$, and $f_f = 0.19$. A four-node linear displacement element with full integration and an edge length of 0.25 mm was used in the center of the tensile bar model. The remaining parameters describing void nucleation were taken from the paper of Needleman and Tvergaard.[A7] This set of parameters characterizing the Gurson model was used to successfully predict J_R-curves from a range of specimen geometries subjected to static and dynamic loading conditions.

Sun et al.[A13] performed a comparative study of the damage models based on the modified Gurson model and on the critical void growth model developed by Rice and Tracey[A14] using the von Mises yield function. Damage parameters were investigated and the local and global behavior of several specimen geometries were compared with experimental data. Both damage models were described as producing qualitatively consistent results with regard to the influence of stress triaxiality on void growth and on the early stages of material failure. Conclusions drawn from the study were that the Gurson model provided a more accurate simulation of material failure after the onset of void coalescence, and the critical crack growth model produced fewer numerical convergence problems in simulating large crack extension.

A.2 Slab-Type Gurson Model

Shih and Xia,[A15] Xia and Shih,[A9] and Ruggieri and Dodds[A16] have idealized the void growth mechanism in a model which assumes that void growth and coalescence are confined to a narrow material layer of initial thickness D, which is centered about the macroscopic fracture plane (see Fig. A.1). They justify this simplification on the basis that many metals which fail by void growth and coalescence exhibit a macroscopically planar fracture process zone of one or two void spacings in thickness. Ligaments between the voids experience intense plastic deformation. Voids which are outside this region are observed to display little or no growth. Within the fracture process zone layer of thickness D, the material response is described by a simplified form of the Gurson micromechanical model. Outside this layer, the material is assumed free of voids and the response to deformation is described by classical J_2 flow theory of plasticity. The overall objective of this approach is to develop an engineering micromechanics model that embodies the essence of stress triaxiality on fracture-toughness, while requiring only a few essential metallurgical parameters.

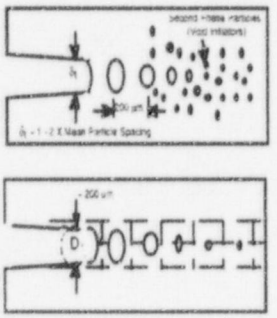

Figure A.1 Ductile tearing by void growth and coalescence with the Gurson local damage model

A further simplification of the Gurson model is introduced by neglecting the evolution equation for void nucleation, leaving only the void growth rate term in Eq. (A.1). (Some implications of void nucleation modeling for fracture predictions can be found in papers by Tvergaard and Hutchinson[A17] and Needleman and Tvergaard.[A7]) The parameters of the Gurson model remaining to be specified are the initial porosity, f_0, the porosity at failure, f_f, the explicit internal length scale, D, which defines dimensions of the computational cells, and the number of finite elements to be defined over D (2-4 elements are thought to be satisfactory). The important microstructural parameters are D and f_0, which can be taken as material parameters and estimated from metallurgical studies of the surfaces of fracture specimens. As an alternative, these parameters can be treated phenomenologically and selected to give the best fit to crack growth data.

Shih and Xia[A15] discretized the process zone with a single row of computational cells having dimensions $D/2 \times D/2$. The Gurson cell is modeled using quadrilateral elements each of which consists of four constant-strain triangular elements. Each cell contains a single void of initial volume fraction f_0, and growth of the void is governed by the stress and strain (computed from the Gurson model) averaged over that cell. Typically, the cell for which $f = 0.1$ is taken as the current position of the advancing crack-tip. A damaged cell is rendered extinct using the element vanishing technique of Tvergaard[A18] when its volume fraction, f, exceeds a critical value, f_f. When this failure condition is reached, the nodal forces computed from the remaining stresses in the now-extinct cell are released in N subsequent solution steps (N is typically 5-20).

Shih and Xia[A15] employ the simplified Gurson material model (SGMM) in finite-element calculations to determine crack growth resistance curves for plane-strain mode-I crack growth under SSY conditions. Values of initial porosity (f_0) ranged from 0.001 to 0.03. Their calculations show that the stress peak and stress distribution in front of the crack-tip are strongly affected by the initial porosity and length of the fracture process zone. For a low initial porosity, strong spatial gradients are computed for both the porosity and the normal stress ahead of the crack-tip. These results are interpreted as being consistent with a single void interacting with the crack-tip, the latter being a fracture mechanism previously studied by Rice and Johnson.[A19] In the case of a higher initial porosity, results indicating less severe gradients in porosity and stress are interpreted as being consistent with multiple interacting voids.

These SGMM fields were shown to be different from those obtained from transient and steady state solutions for growing cracks that do not include damage and material softening in their calculations (such as Varias and Shih[A20] and O'Dowd, Shih and Dodds[A21]). For low initial porosities, material softening was found to reduce the normal stress in the fracture process zone, but to cause an elevation immediately outside the process zone; the latter redistribution of stress was not found in Refs. A20 and A21. This result is cited as indicating a possible drawback for those analysis procedures that do not include material softening, such as node release techniques.

The SGMM was employed to compute J-resistance curves for deep- and shallow-crack bend bars previously tested by Joyce.[A22] Applications using damage parameters given by $D/2 = 100$ microns and $f_0 = 0.005$ ($f_f = 0.2$) successfully reproduced the experimentally measured J-Δa curves for both the shallow and deep-crack bend bars. Results from these calculations are used to address the competition between ductile tearing and unstable cleavage fracture in the transition temperature region. Their discussion focuses on the argument that the stress elevation caused by crack growth is one of several factors contributing to the transition to cleavage fracture after some amount of stable ductile crack growth. It is suggested that the SGMM can be used in combination with a statistical cleavage fracture model and a proper length scale to predict the transition to cleavage fracture after some amount of ductile tearing. A procedure is proposed for calibrating the parameters of such a combined ductile/cleavage computational model. A combined testing/analytical program would utilize high constraint specimens (i.e., no ductile tearing) to determine parameters for the cleavage model, while low constraint geometries would provide data incorporating substantial ductile tearing for calibration of D and f_0. The calibrated model would then be used to predict fracture behavior in a third geometry which exhibits some amount of pre-cleavage tearing.

In a later study, Xia, Shih and Hutchinson[A23] select the two parameters, D and f_0, using a phenomenological approach, i.e., the parameters are adjusted to give the best fit for one set of experimental crack growth data for a specific material. In applications of the model to specific materials, it is recommended in Ref. A23 that the analyst first choose a sub-element discretization scheme for the Gurson slab on the fracture plane. In the second step, D and f_0 are selected to best reproduce the experimental data for the material. The sub-element discretization and parameters D, f_0 are then transferred to different specimen geometries of the same material. The latter technique was applied in Ref. A23 to model ductile crack growth in specimens of A 533 B and A 710 steels, using as many as five different specimen geometries (i.e., three-point bend, compact tension, double-edge-notch tension strip, single edge-notch tension strip, and center crack panel).

Ruggieri and Dodds[A16] have incorporated the SGMM into the finite-element computer program WARP3D[A24] which is under development at the University of Illinois. Descriptions of the WARP3D program emphasize a solution strategy employing an implicit element-by-element, preconditioned conjugate-gradient algorithm. The computational scheme is implemented to execute in parallel/vector mode for the efficient solution of large-scale, three-dimensional (3-D) finite element models. The WARP3D program is described as offering a range of nonlinear constitutive models (in addition to Gurson), a domain integral formulation for J-integral calculations, various procedures for crack growth modeling, and a global dynamic analysis capability.

Applications[A16] of the WARP3D model for ductile crack growth were described for an SSY model (with $T = 0$) and for a deeply-notched SENB specimen ($a/W = 0.6$), based on properties typical of a moderate strength pressure vessel steel.[A24] The focus of these analyses was on the capabilities of the model to predict J-resistance curves for a range of initial void volume fraction values under both small-scale and large-scale yielding conditions. According to Ruggieri and Dodds,[A16] crack growth by ductile tearing would be anticipated for relatively large initial porosity (for example, $f_0 = 0.01$) because the high stresses necessary for cleavage initiation could not be achieved near the crack-tip. As the porosity is lowered (for example, to $f_0 = 0.001$), a transition to the cleavage mode is expected to be favored because the stresses ahead of the crack-tip would be significantly higher and the high stress region would extend over a larger region. Since the role of void nucleation is neglected in the SGMM, it is anticipated that the SGMM will perform better for materials characterized by larger initial porosities (such as low-to-mid strength structural and pressure vessel steels).

The explicit length scale D was set at 0.2 mm, the critical volume fraction at $f_f = 0.2$, and values of f_0 ranged from 0.001 to 0.01, to allow comparisons of results with recent plane-strain analysis of Xia and Shih.[A9] In Ref. A16, D and f_0 are regarded as computational parameters which are loosely coupled with specific metallurgical features of the material such as mean spacing of particles. Mesh models used in the analyses employed 8-node, 3-D isoparametric elements incorporating a finite strain formulation. Plane strain constraints were imposed on the 3-D elements to facilitate comparisons with results of Xia and Shih.[A9]

Analysis results for an amount of crack growth equal to D in the SSY model indicate that near-tip stresses demonstrate an inverse dependence on initial porosity. Thus, a low initial value for the void volume fraction leads to higher stresses and to larger regions near the crack-tip which are subjected to higher tensile stresses. Before the onset of crack growth, stresses ahead of the tip are reduced in magnitude due to blunting of the crack-tip. Crack growth restores the higher stresses and increases the distance ahead of the crack-tip over which the higher stresses occur. This feature of the stress fields associated with ductile tearing has implications for fracture-mode conversion in the transition temperature region. In particular, for materials with initially low void volume fraction, conversion to cleavage becomes more likely during the ductile crack growth process.

The model for the SENB specimen used to predict a J-Δa curve provided somewhat lower J-values than the experimental data. This result was attributed to the effects of using values for the computational parameters D, f_0 that were previously calibrated numerically by Xia and Shih[A9] using a stiffer model.

Appendix A References

A1. A. L. Gurson, "Continuum Theory of Ductile Rupture by Void Nucleation and Growth: Part I — Yield Criteria and Flow Rules for Porous Ductile Media," *J. Engng. Mater. Tech.* **99**, 2–15 (1977).

A2. W. Brocks, D. Klingbeil, G. Künecke, and D. -Z. Sun, "Application of the GURSON Model to Ductile Tearing Resistance," *Constraint Effects in Fracture: Theory and Application*, ASTM STP 1244, Philadelphia, PA, 1994.

A3. A. Needleman and J. R. Rice, "Limits to Ductility by Plastic Flow Localization," *Mechanics of Sheet Metal Forming*, (eds. D. P. Koistinen and N. -M. Wang), Plenum Publishing Company, New York, pp 237–265, 1978.

A4. C. C. Chu and A. Needleman, "Void Nucleation Effects in Biaxially Stretched Sheets," *J. Engng. Mater. Tech.* **102**, 249–256 (1980).

A5. V. Tvergaard and A. Needleman, "Analysis of the Cup-Cone Fracture in a Round Tensile Bar," *Acta. Metall.* **32**, 157–169 (1984).

A6. A. Needleman and V. Tvergaard, "An Analysis of Ductile Rupture in Notched Bars," *J. Mech. Phys. Solids* **32**, 461–490 (1984).

A7. A. Needleman and V. Tvergaard, "An Analysis of Ductile Rupture Modes at a Crack Tip," *J. Mech. Phys. Solids* **35**, 151–183 (1987).

A8. V. Tvergaard, "On Localization in Ductile Materials Containing Spherical Voids," *Int. J. Fract.* **18**, 237–252 (1982).

A9. L. Xia and C. F. Shih, "Ductile Crack Growth —I. A Numerical Study using Computational Cells with Microstructurally-Based Length Scales," *J. Mech. Phys. Solids* **43**, 233-259 (1995).

A10. J. Pan, M. Saje, and A. Needleman, "Localization of Deformation in Rate Sensitive Porous Plastic Solids," *Int. J. Frac.* **21**, 261–278 (1983).

A11. A. Needleman and V. Tvergaard, "An Analysis of Dynamic Ductile Crack Growth in a Double Edge Cracked Specimen," *Int. J. Frac.* **49**, 41–67 (1991).

A12. D -Z. Sun, A. Hönig, W. Böhme and W. Schmitt, "Application of Micromechanical Models to the Analysis of Ductile Fracture under Dynamic Loading," *Fracture Mechanics: 25th Volume, ASTM STP 1220*, (Eds. F. Erdogan R. J. Hartranft), 1994.

A13. D. Z. Sun, D. Siegele, B. Voss, and W. Schmitt, "Application of Local Damage Models to the Numerical Analysis of Ductile Rupture," *Fatigue Fract. Engng. Mater. Struct.* **12**(3), 201-212 (1989).

A14. J. R. Rice and D. M. Tracey, "On the Ductile Enlargement of Voids in Triaxial Stress Fields," *J. Mech. Phys. Solids* **17**, 201-217 (1969).

A15. C. F. Shih, and L. Xia, "Modeling Crack Growth Resistance Using Computational Cells with Microstructurally-Based Length Scales," *Constraint Effects in Fracture: Theory and Application*, ASTM STP 1244, Philadelphia, Pennsylvania, 1994.

A16. C. Ruggieri and R. H. Dodds, Jr., "Numerical Modeling of Ductile Crack Growth in 3-D Using Computational Cell Elements," *Int. J. Fract.* **82**, 67-95 (1996).

A17. V. Tvergaard and J. W. Hutchinson, "Effect of T-Stress on Mode I Crack Growth Resistance in a Ductile Solid," *J. Mech. Phys. Solids*, **40**, 1377–1397 (1992).

A18. V. Tvergaard, "Influence of Void Nucleation on Ductile Shear Fracture at a Free Surface," *J. Mech. Phys. Solids* **30**, 399-425 (1982).

A19. J. R. Rice and M. A. Johnson, "The Role of Large Crack Tip Geometry Changes in Plane Strain Fracture," *Inelastic Behavior of Solids*, Eds. M. F. Kanninen, W. F. Adler, A. R. Rosenfeld and R. I. Jaffee, McGraw-Hill, New York, 641-672 (1970).

A20. A. G. Varias and C. F. Shih, "Quasi-Static Crack Advance under a Range of Constraints-Steady-State Fields Based on a Characteristic Length," *J. Mech. Phys. Solids* **41**, 835-861 (1993).

A21. N. P. O'Dowd, C. F. Shih, and R. H. Dodds,Jr., "The Role of Geometry and Crack Growth on Constraint and Implications for Ductile/Brittle Fracture," in *Constraint Effects in Fracture: Theory and Applications, ASTM STP 1244*, M. Kirk and A. Bakker, Eds., American Society for Testing and Materials, Philadelphia, 1994.

A22. J. A. Joyce, "Effects of Tensile Loading on Upper Shelf Fracture Toughness," Presented at Constraint Workshop, Anapolis, MD, February 11-12, 1993.

A23. L. Xia, C. F. Shih, and J. W. Hutchinson, Division of Applied Sciences, Harvard University, "A Computational Approach to Ductile Crack Growth under Large Scale Yielding Conditions," Mech-236, June 1994.

A24. K. C. Koppenhoefer, A. S. Gullerud, C. Ruggieri, R. H. Dodds, Jr., and B. E. Healy, Department of Civil Engineering, University of Illinois, "WARP3D: Dynamic Nonlinear Analysis of Solids using a Preconditioned Conjugate Gradient Software Architecture," UILU-ENG-94-2017, November 1994.

NRC FORM 335 (2-89) NRCM 1102, 3201, 3202

U.S. NUCLEAR REGULATORY COMMISSION

BIBLIOGRAPHIC DATA SHEET

(See instructions on the reverse)

1. REPORT NUMBER (Assigned by NRC, Add Vol., Supp., Rev., and Addendum Numbers, if any.)

NUREG/CR-6380
ORNL/TM-13091

2. TITLE AND SUBTITLE

Assessment of the Fracture Behavior of Weld Material in Full-Thickness Clad Beams

3. DATE REPORT PUBLISHED

MONTH	YEAR
July	1999

4. FIN OR GRANT NUMBER

B0119

5. AUTHOR(S)

J. A. Keeney, B. R. Bass, W. J. McAfee, and P. T. Williams

6. TYPE OF REPORT

7. PERIOD COVERED (Inclusive Dates)

8. PERFORMING ORGANIZATION – NAME AND ADDRESS (If NRC, provide Division, Office or Region, U.S. Nuclear Regulatory Commission, and mailing address; if contractor, provide name and mailing address.)

Oak Ridge National Laboratory
Oak Ridge, Tennessee 37831-6285

9. SPONSORING ORGANIZATION – NAME AND ADDRESS (If NRC, type "Same as above"; if contractor, provide NRC Division, Office or Region, U.S. Nuclear Regulatory Commission, and mailing address.)

Division of Engineering Technology
Office of Nuclear Regulatory Research
U. S. Nuclear Regulatory Commission
Washington, DC 20555-0001

10. SUPPLEMENTARY NOTES

S. N. Malik, NRC Project Manager

11. ABSTRACT (200 words or less)

A Heavy-Section Steel Technology testing program was conducted on full-thickness clad beam specimens fabricated using material from the reactor pressure vessel of a canceled nuclear power plant to generate fracture toughness data for both deep and shallow cracks in prototypic RPV material. The beam specimens incorporated weld, base, and overlay cladding materials. In the first testing phase, five full-thickness clad beam specimens were fabricated with through-thickness cracks that ranged in depth from 10 to 114 mm ($0.05 \leq a/W \leq 0.5$) in the weld material. These specimens were tested in three-point bending at temperatures in the transition region of the weld metal fracture toughness curve. Fracture toughness estimates were obtained from load versus load-line displacement and crack-mouth opening displacement data using finite-element techniques and estimation schemes based on the η-factor method. Effects of precleavage ductile tearing on fracture toughness were investigated using a continuum damage model based on the Gurson-Tvergaard formulation. The cleavage toughness data were compared with other shallow- and deep-crack uniaxial beam data generated previously from plate material that conformed to SA533, Grade B material specification requirements. The range in scatter for data obtained from the clad beam specimens is consistent with that from the laboratory-scale single-edge-notched-bend specimens tested at the same temperature.

12. KEY WORDS/DESCRIPTORS (List words or phrases that will assist researchers in locating the report.)

A533 Grade B Class 1 steel
Full-thickness clad beam
Shallow-crack beam
Constraint analysis
Furson-Tvergaard Model
Elastic-plastic fracture mechanics
Fracture toughness data
Precleavage ductile tearing
J-Q Methodology
Compact tension specimen

13. AVAILABILITY STATEMENT

Unlimited

14. SECURITY CLASSIFICATION

(This Page)
Unclassified

(This Report)
Unclassified

15. NUMBER OF PAGES

16. PRICE

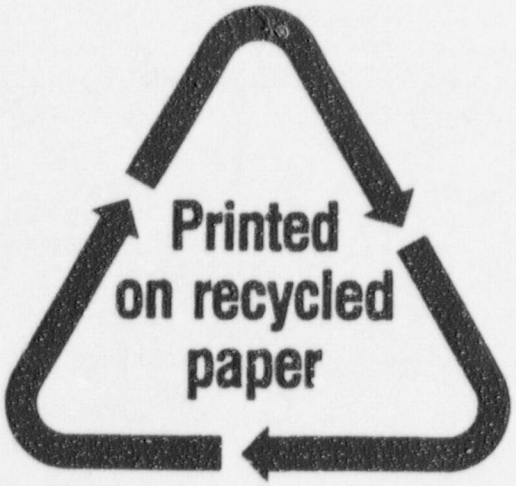

Federal Recycling Program

UNITED STATES
NUCLEAR REGULATORY COMMISSION
WASHINGTON, DC 20555-0001

OFFICIAL BUSINESS
PENALTY FOR PRIVATE USE, $300

FIRST CLASS MAIL
POSTAGE AND FEES PAID
USNRC
PERMIT NO. G-67